# MICROFABRICATED WATER-IMMERSIBLE SCANNING MIRRORS FOR ULTRASOUND AND PHOTOACOUSTIC IMAGING

A Dissertation

by

SONG XU

Submitted to the Office of Graduate and Professional Studies of
Texas A&M University
in partial fulfillment of the requirements for the degree of

DOCTOR OF PHILOSOPHY

| | |
|---|---|
| Chair of Committee, | Jun Zou |
| Committee Members, | Raffaella Righetti |
| | Sheng-Jen 'Tony' Hsieh |
| | Paotai Lin |
| Head of Department, | Miroslav M. Begovic |

May 2019

Major Subject: Electrical Engineering

# ABSTRACT

Scanning acoustic microscopy (SAM) and photoacoustic microscopy (PAM) techniques have been attracting attention over the past few decades because of their non-invasive and non-ionizing nature. However, current desk-top SAM and PAM systems utilizing mechanical stages are usually bulky and thus difficult to be miniaturized as hand-held or endoscopic probes. In recent years, MEMS (microelectromechanical system) technology has been applied to develop other optical microscopy systems: confocal microscopy and optical coherent microscopy. However, these MEMS devices are not suitable for SAM or PAM systems because liquid environment is necessary for ultrasound propagation.

The work in this dissertation focuses on the development of reliable water-immersible scanning mirrors with polymer torsional hinges using micromachining technology. First, a new water--immersible two-axis scanning mirror driven by multiple actuators is proposed and prototype is fabricated. The prototype is able to provide predictable, reliable and repeatable raster scanning pattern in both air and water. Second, combining 3D printing mounting structures, a miniaturized single-axis scanning mirror driven by single actuator is fabricated and characterized. Furthermore, in order to miniaturize the package size of the water-immersible two-axis scanning mirror, innovations have been made from both designing principle and fabrication technique perspectives. In the third prototype, it is possible to achieve two-axis scanning with single actuator through dynamic filtering principle. Therefore, the package size and module complexity can be reduced. Lastly, a high resolution polymer fabrication recipe is developed for the fourth prototype. With high structural resolution, the overall package size is reduced from $16 \times 16 \times 13\ mm^3$ to $5 \times 5 \times 5\ mm^3$. At the same time, since the fabrication process is based on common MEMS treatment methods and minimal manual assemble involved, it is possible to batch fabricate this prototype, further reducing the cost of each piece.

CONTRIBUTORS AND FUNDING SOURCES

## Contributors

This work was supported by a dissertation committee consisting of Professor Jun Zou, Professor Raffaella Righetti, and Professor Paotai Lin of the Department of Electrical and Computer Engineering and Professor Sheng-Jen 'Tony' Hsieh of the Department of Engineering Technology and Industrial Distribution.

All other work conducted for the dissertation was completed by the student independently.

## Funding Sources

Graduate study was supported by National Science Foundation IDBR 1255921.

TABLE OF CONTENTS

Page

LIST OF FIGURES

FIGURE Page

# LIST OF TABLES

TABLE Page

# 1. INTRODUCTION

## 1.1 Motivation

With the development of biomedical imaging science, clinical diagnoses and academic researches are depending more and more on imaging technologies including but not limited to computer tomography (CT), magnetic resonance imaging (MRI), ultrasonography, infrared thermography, and photoacoustic imaging. Among these imaging techniques, scanning acoustic microscopy (SAM) and newly developed photoacoustic microscopy (PAM) are drawing attentions because of their non-invasive and non-ionizing nature.

In both SAM and PAM systems, the samples can be mapped by motor stages. This approach provides as many 'pixels' as possible, ensuring a very high resolution. But a significant drawback of this mapping or beam steering strategy is that they make the system either complex or bulky. In ultrasound imaging, another important beam steering method is to use phased arrays. By programming the trigger signals of 16 to 128, sometimes as many as 256, transducers, the ultrasound beam shape and focus can be adjusted. Therefore, sample mapping becomes possible. This approach enables good controllability over the beam shape and focal spot position. But integrating multiple transducers in one probe inevitably makes the system complex and expensive.

In optical microscopy, there is another important beam steering method: MEMS scanning mirrors. These MEMS mirrors usually have very small feature sizes, fast scanning speed; and the cost of each device is usually very low since they can be batch fabricated. Integrating them into optical microscopy systems significantly reduced the systems size and complexity. This beam steering idea could be transferred to SAM and PAM systems and, as a result, the overall system size and complexity can also be reduced.

## 1.2 Opportunities and Challenges

It would be beneficial to integrate MEMS scanning mirrors with SAM and PAM systems in many perspectives. First, the cost can be reduced. Only one transducer is needed to couple with

MEMS scanning mirror rather than multiple elements in phased transducer array. Second, system size can be reduced. If the stages were replaced by a MEMS scanning mirror, all photoacoustic scanning components (fiber, lenses, mirror, prism and transducer) can be integrated in a compact probe. The overall size will be greatly reduced, making handheld photoacoustic imaging devices, even endoscopic probes, possible. Third, mechanically actuated stages are slow in response rate compared with MEMS scanning mirrors. It is difficult to achieve real-time imaging utilizing these mechanical stages. However, this will be different for the case of MEMS scanning mirrors. MEMS scanning mirrors have a wide range of working frequencies:from a few hundred Hz to kHz [22]. It is possible to realize *in vivo* imaging with photoacoustic techniques.

Traditional MEMS scanning mirrors are not suitable for SAM or PAM systems. Both systems involve ultrasound transmission: SAM system relies on backscattered ultrasound signals to reconstruct images; PAM system collects thermo-acoustic signals to map the target. Liquid environment (water in most cases) is essential for the propagation of ultrasound signals. However, most of current MEMS scanning mirrors are designed for operations in air: their performances in liquid cannot be trusted. Conventional MEMS scanners are usually fabricated from silicon wafer because the fabrication techniques of silicon have been well studied. In order to achieve a relatively large scanning angle, these silicon torsional hinges are usually designed in a slender fashion. When immersed in water, these slender torsional hinges are susceptible to permanent damage from a small turbulence or shock, which are often encountered in a liquid environment.

### 1.3 Thesis Outline

The work in this thesis is focused on designing and fabricating reliable water-immersible two--axis scanning mirrors and miniaturizing their package sizes. Chapter 2 discusses the principle of SAM and PAM; the state-of-art of current MEMS mirrors; and previous researches on water--immersible scanning mirrors. By optimizing the design of the previous prototype, performance reliability can be significantly improved. To prove this, a prototype is fabricated and characterized in Chapter 3. The following three chapters focus on feature size miniaturization. In Chapter 4, a new structural layout is proposed to miniaturize the package size without losing numerical

aperture. In Chapter 5, a novel actuation mechanism based on dynamic filtering effect is presented. Through this method, the number of actuators is reduced to one, opening the possibility of further miniaturization. In Chapter 6, high resolution fabrication process is developed. Combining the new actuation mechanism and fabrication process, a miniaturized two-axis water-immersible scanning mirror prototype is finally prepared. The package size is reduced from 16 $\times$ 16 $\times$ 13 $mm^3$ to 5 $\times$ 5 $\times$ 5 $mm^3$, comparable to commercial MEMS scanners in optical microscopy. The last piece of work in Chapter 7 focuses on increasing the field of view through hybriding different scanning modes. In Chapter 8, we draw the conclusions and propose future extensions of this work.

# 2. BACKGROUND AND STATE-OF-ART

## 2.1 Introduction of Scanning Acoustic Microscopy and Photoacoustic Microscopy

Since the first published microelectromechanical system (MEMS) scanner [23], MEMS scanning mirrors have been providing solutions to beam steering in many different applications: confocal microscopy [24, 25], optical coherence spectroscopy (OCT) [26, 27], retinal scanning display (RSD) [28], and light detection and ranging (LiDAR) [29, 30].

The first scanning acoustic microscope was introduced in [31]. Many improvements to this systems has been made to enhance the resolution and accuracy. In SAM system, a focused transducer (Fig. 2.1) is used to fires focused ultrasound pulses. The altitude of the sample is adjusted such that the target is located in the focal zone of the transducer. The sound pulses hitting the sample is either scattered, absorbed reflected or transmitted. The backscattered ultrasound pulses are collected by the transducer. The time between the fired signal and backscattered signal is defined as "time of flight". The time of flight can be used to calculate the distance between the target and the transducer given the speed of sound in the medium. Also, the amplitude of backscattered signal carries the information of acoustic impedance. By moving the transducer to different locations and repeating the above process, the acoustic impedance of the target can be mapped and the depth of the target can be decided. Fig. 2.2 shows the schematic system of SAM. Ultrasound has been proved to be a powerful tool in studying elastography [32, 33]. Because of the high resolution, SAM is capable of providing elasticity of cells or tiny tissues. The change of elasticity reveals the information of the physical forces holding structures in a particular shape and the mechanics of structure [34, 35], which has been widely utilized in medicine and biology researches [36, 37].

Photoacoustic microscopy is an imaging method based on photoacoustic effect [38]. Laser beam firstly fired onto the targets. Photoacoustic microscopy takes the advantage of the local temperature rise that occurs as a result of light absorption in the target. Undergoing thermoelastic expansion, wide band acoustic wave is therefore generated and detected by high frequency trans-

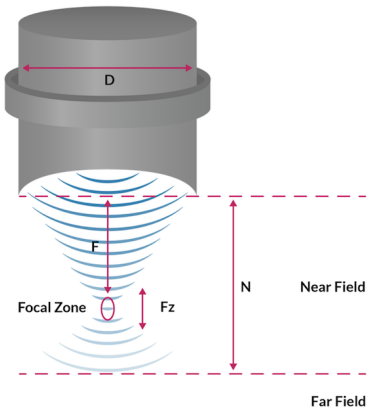


Figure 2.1: A focused transducer.

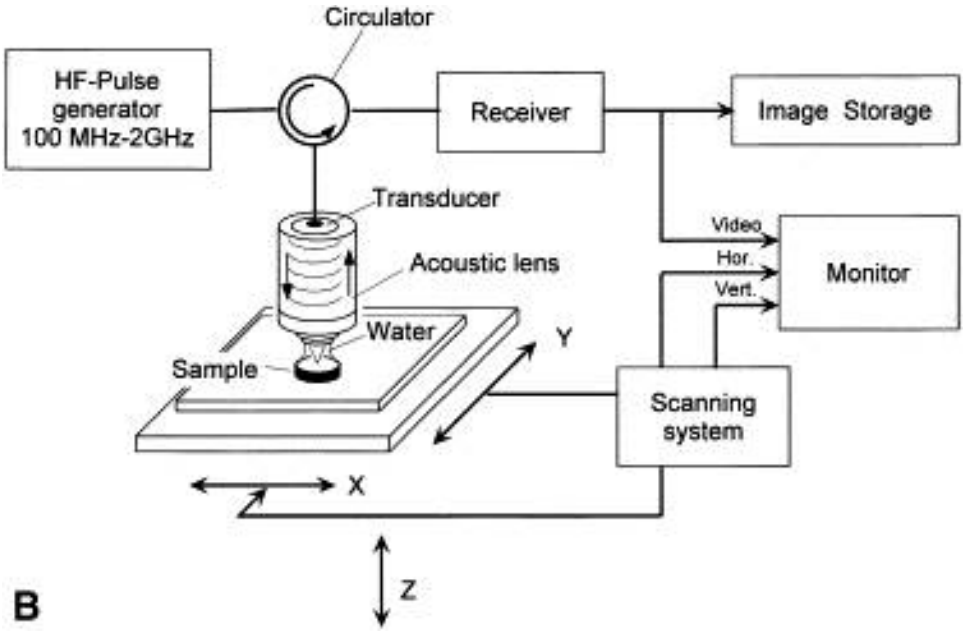


Figure 2.2: A schematic drawing of SAM system.

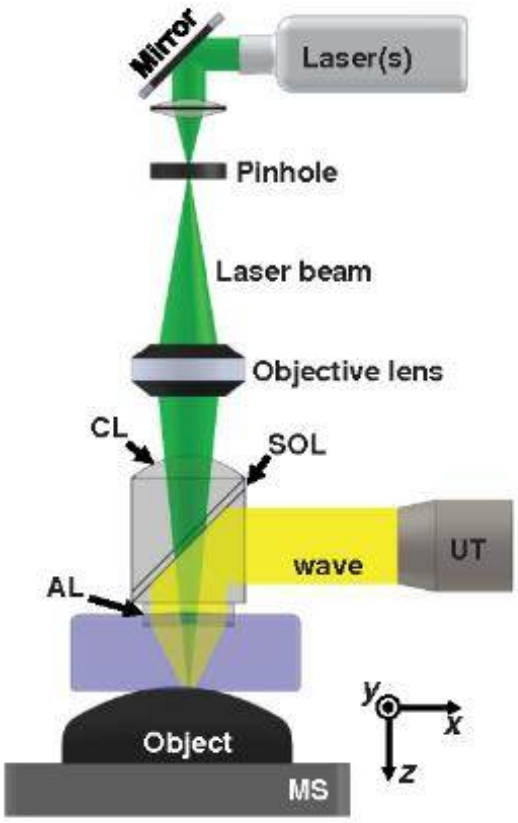


Figure 2.3: Schematic drawing of PAM scanning head.

ducers. Because the scattering of ultrasound signals in tissues is usually weaker than that of optical signals, photoacoustic microscopy is capable of capturing high resolution images at higher depth than conventional optical microscopy methods [39, 40]. Fig. 2.3 shows the layout of photoacoustic microscopy scanning head [41]. Then this imaging head is moved to another location [42] and the above procedures are repeated to acquire the photoacoustic signals (Fig. 2.4). After mapping out the sample, a photoacoustic image can be reconstructed.

It can be noticed that in both Fig. 2.2 and Fig. 2.4, the scanning heads in both SAM and PAM systems have to be moved to different locations on the target to finish the mapping (beam steering). In PAM systems, the scanning head (comprised of a laser head and transducer) is usually mounted on a mechanical x-y linear stage [43]. Besides mechanical stages, ultrasound beam steering in SAM systems is sometimes achieved by phased transducer arrays [44]. The phased transducer

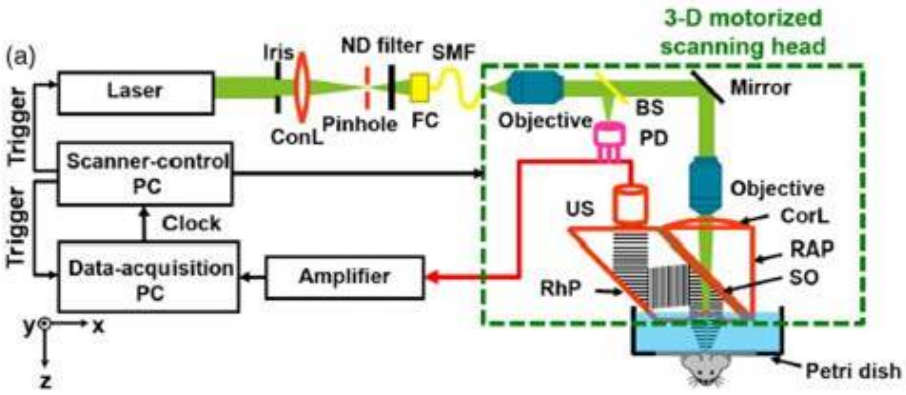


Figure 2.4: Schematic drawing of PAM system.

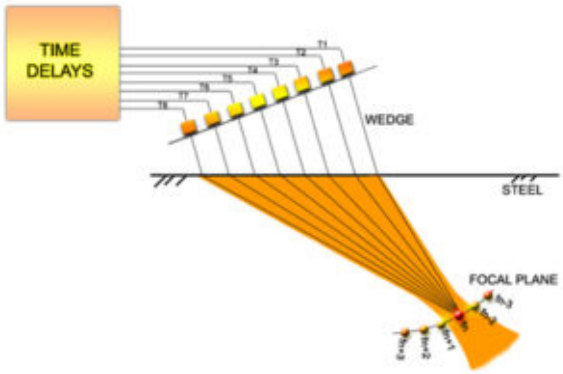


Figure 2.5: Schematic drawing of phased transducer array.

array [45] is consisted of many small ultrasound transducer elements (Fig. 2.5), each of which can be pulsed independently. By varying the timing, for instance by pulsing the elements one by one in sequence along a row, a pattern of constructive interference is set up that results in a beam at a set angle. By programming the triggering signals, ultrasound beam fired from the transducer array is able to sweep through the tissue or object being examined.

## 2.2 State-of-Art of MEMS Scanning Mirrors

In recent few years, MEMS scanning mirrors have been studied and developed to meet various applications. MEMS scanners have been an integral part of MEMS research for more than three decades. Depending on different actuation mechanisms, conventional MEMS scanning mirrors

can be roughly classified into four categories: electrostatic, thermoelectric, piezoelectric, and electromagnetic. In this part, the working principles, advantages and disadvantages of electrostatic, thermoelectric, piezoelectric, and electromagnetic MEMS scanners will be discussed.

Due to its versatility, electrostatic sensing and actuation is a candidate for almost all category of sensor and actuator product [46]. Using electrostatic actuators, there are several advantages. Simplicity: only two conductive surfaces are needed (on the contrary, piezoelectric actuators requires piezoelectric material and thermoelectric driving requires materials with different thermal expansion coefficients). Low power consumption in static and low-frequency: since electrostatic actuation relies on voltage differential rather than current, in static, the power consumption is zero. Fast response time: governing by capacitance charging and discharging time constant, the response time can be designed very small. The electrostatic actuators operates in a similar fashion of parallel-plate capacitor. Assuming one of the capacitor plate is suspended or deformable, another one firmly anchored. As a differential voltage is applied between the two parallel plates, an electrostatic attraction force will develop, actuating the MEMS scanning mirror [47, 48].

An governing equation of the force, $F$, between a parallel plate capacitor is [49]:

$$F = \frac{1}{2}\frac{CV^2}{d} \tag{2.1}$$

where $C$ is the capacitance, $V$ is the applied voltage, and $d$ is the distance between two parallel plates.

There are two typical types of MEMS scanning mirrors based on electrostatic actuation: parallel--plate [1] and come-drive capacitors [2]. In Fig. 2.6, the parallel capacitor is form between mirror mirror address electrode and the yoke address electrode. Comb-drive capacitors are more widely used in MEMS scanners because of larger surface area, and therefore electrostatic force (Fig. 2.7).

Parallel-plate MEMS scanners can be fabricated with a standard foundry process. However, since the moving electrode (mirror plate) has to be separated from the fixed electrode (substrate), lift-up assembly procedure has to be included. One approach is to use a microactuated 3-D struc-

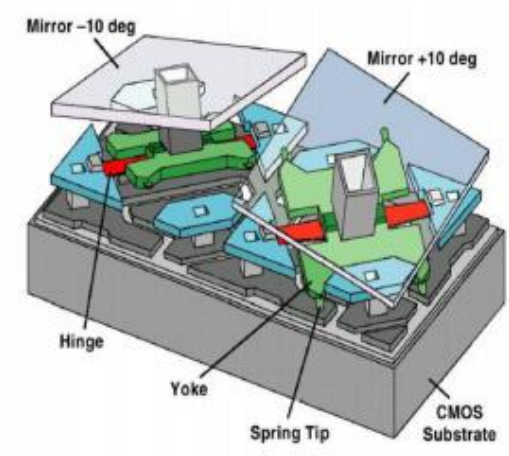


Figure 2.6: MEMS scanner based on parallel plate. Reprinted from [1]

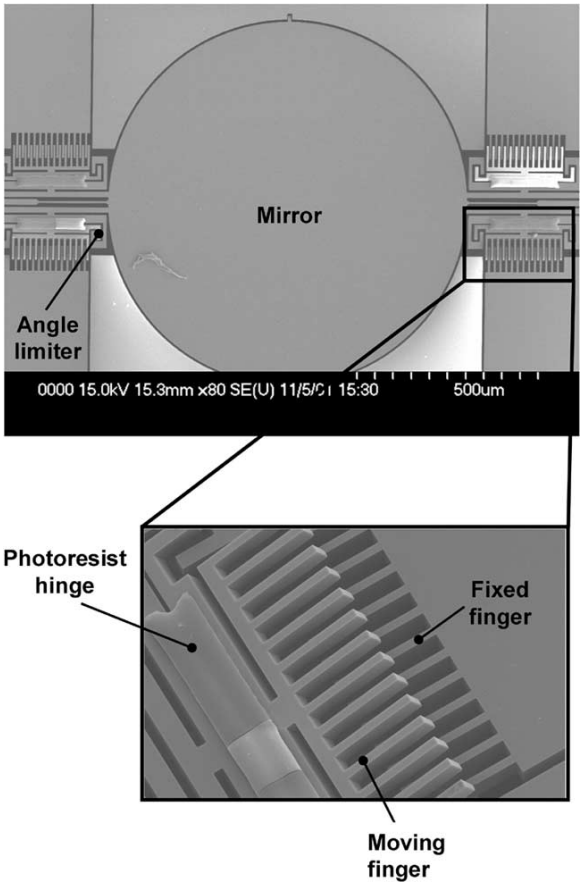


Figure 2.7: MEMS scanner based on comb-drive. Reprinted from [2]

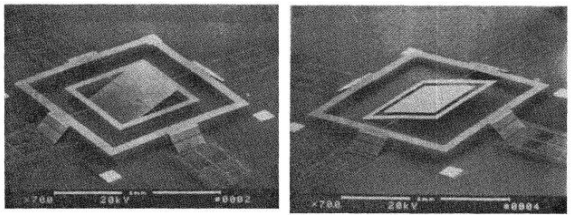

Figure 2.8: MEMS scanner based on parallel plate realized by MESA method. Reprinted from [3]

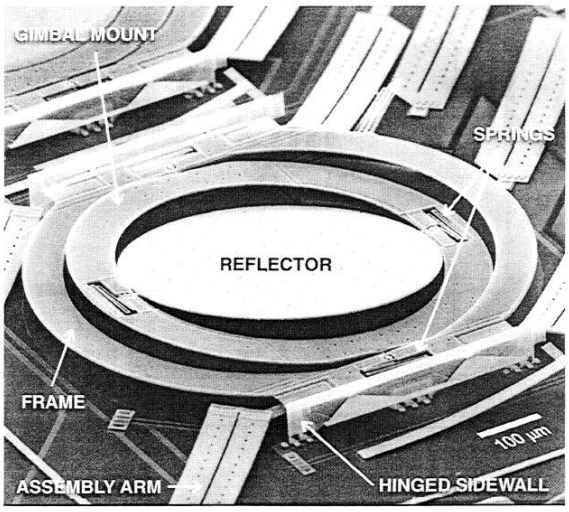


Figure 2.9: MEMS scanner based on parallel plate utilizing the residual stress. Reprinted from [4]

ture called micro-elevator by self-assembly (MESA) [2]. Adopting this approach, Fan and Wu [3] lifted the polysilicon mirror plate vertically 200 $\mu m$ above to realize two-axis scanning (Fig. 2.8). Another important approach is to utilize the residual stress in deposited thin films (Cr or Au on polysilicon) to achieve leviation [4, 50]. As noticed in Fig. 2.9, the frame is above the substrate to create a gap to form a parallel-plate capacitor.

Comb-drive electrostatic MEMS mirrors can be further classified into two subjects: lateral comb-driving (firstly demonstrated by Tang [51]), and more prevalent vertical comb-driving (firstly introduced by Schenk [52]). There are several advantages that can be offered by vertical comb--drive actuators. First, the mirror plate is not directly fabricated on the actuator. Therefore, the maximum scanning angle is no longer limited by the geometric size of the parallel plate. Moreover,

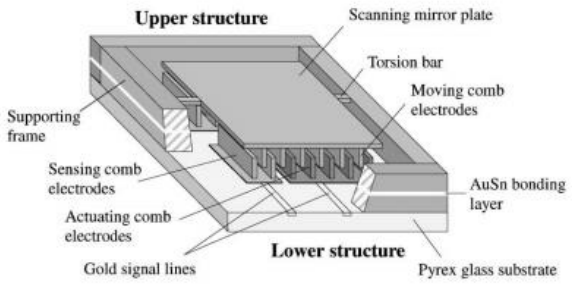


Figure 2.10: Directly integrating the mirror plate to the comb-drive actuator. Reprinted from [5]

pull-in effect can be avoided using vertical comb-drive actuators. The pull-in condition can be defined as at which point the mechanical contact force will finally balance the electric one. Further reducing the distance, the parallel plate will snap onto each other [53, 54, 55].

The comb-drive actuators are composed of two sections: fixed combs and moving combs. The challenge in fabrication is to combine the comb-drive actuators with the mirror plates. Recent efforts have been focused on the development of self-aligned processes or device structures. In [5], the movable comb is directly integrated underneath the mirror plate. As shown in Fig. 2.10, the fixed and movable combs were fabricated in two separate single crystal silicon layers. Then these two combs were bonded together with a gold-tin layer utilizing a flip-chip aligner. Lastly, the bottom silicon layer was anodically bonded to glass before the fixed combs were etched. Krisnamoorthy and Solgaard [56, 57] provide the self-aligned vertical comb-drive fabrication process by utilizing sacrificial comb teeth such that the final etch defines both the fixed and moving comb. Another self-aligned process with angular vertical comb-drive has been proposed by [6]. As shown in Fig. 2.11, once the thermaoplastic hinge heated, the moving combs are rotated out of the wafer plane.

The thermal bimetallic effect is a very commonly used method for sensing and actuation. Thermoelectric actuators usually consist of at least two layers of materials having different coefficients of thermal expansion (CTE). With a temperature rise, the length of these two sections changes unequally. Because the two-layered materials are tightly joined at the interface, the beam must curve toward the layer with lower CTE, actuating the module [58, 59].

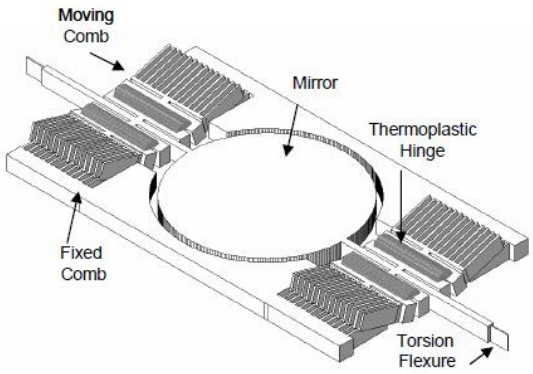


Figure 2.11: Self-aligned angular vertical comb-drive micromirror. Reprinted from [6]

The radius of curvature of the arc, $r$, can be calculated using this formula [60]:

$$\frac{1}{r} = \frac{6w_1w_2E_1E_2t_1t_2(t_1+t_2)(\alpha_1-\alpha_2)\Delta T}{(w_1E_1t_1^2)^2+(w_2E_2t_2^2)^2+2w_1w_2E_1E_2t_1t_2(2t_1^2+3t_1t_2+2t_2^2)} \tag{2.2}$$

The subscript refers to the material layer. The coefficients of thermal expansion, Young's modulus, width, and thickness of the two layers are denoted $\alpha_i$ $E_i$, $w_i$, and $t_i$ $(i = 1, 2)$. $\Delta T$ is the temperature rise. Fig. 2.12 shows an example of thermal bimorph MEMS scanner with schematic draws of the hinges [7]. By increasing the number of bimorph actuators (Fig. 2.13), the MEMS scanner can be more robust [8]. Due to the inherently long response time of electrothermal devices, scanners based on this technology is usually combined with other actuation mechanisms to drive slow-axis [61, 62].

In order to improve the mechanical deflection performance, electrothermal bimorph actuators have evolved from traditional straight actuators to curved actuators [9]. As shown in Fig. 2.14, the mechanical deformation of the mirror plate is dependent on the length of the electrothermal actuator, these curved actuators significantly increased the length without increasing the overall size of the module. In order to increase the fill-factor and robustness of the micromirror, Jia [10] proposed a method to hide the thermal actuators underneath the mirror plate, which are also protected by the silicon sidewalls (Fig. 2.15). This feature is important when integrating a large number of micromirrors to form an array.

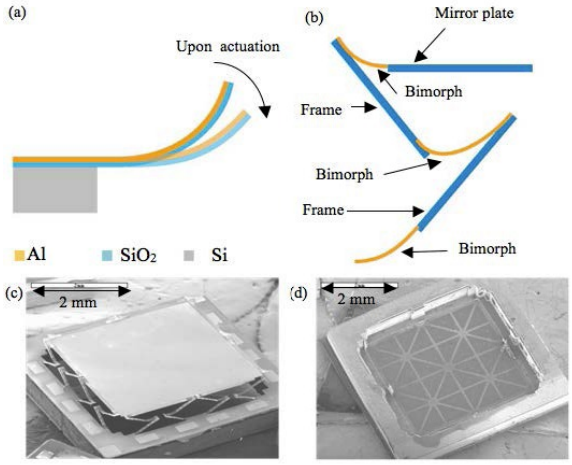


Figure 2.12: MEMS scanner actuated by thermal bimorph actuators. Reprinted from [7]

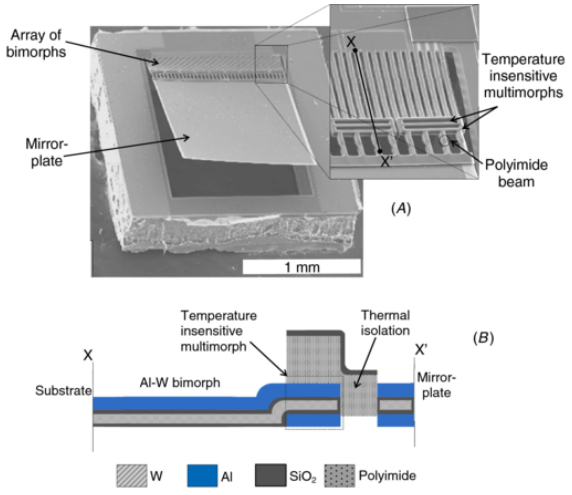


Figure 2.13: Multiple thermal actuators arranged in an array to increase the robustness. Reprinted from [8]

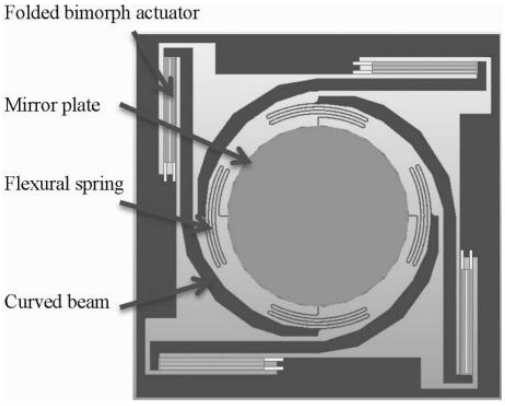


Figure 2.14: Top view of a 3-D model of a two-axis electrothermal actuated MEMS mirror. Reprinted from [9]

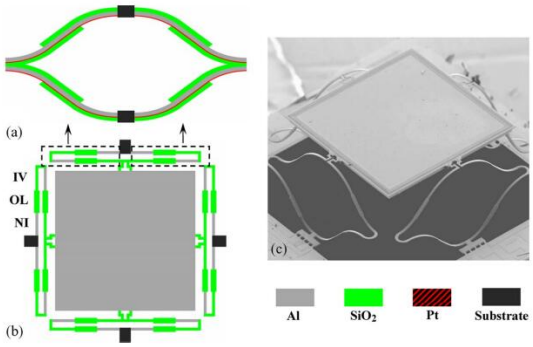


Figure 2.15: Cross section view and SEM image of the electrothermal micromirror device with high fill-in-factor. Reprinted from [10]

The principle of piezoelectric actuation lies in the microscopic piezoelectricity. An external electric field changes the spacing between positive and negative charge sites in piezoelectric materials, therefore, leading to an elastic stress (tensile or compressive depending on the field polarity) [63, 64]. A simplified analytical module of cantilever piezoelectric actuator is consisted of two layers of the same length, one elastic and one piezoelectric. For simplicity, the induced stress and strain are along the longitudinal axis of the cantilever. The beam bends into an arc when the piezoelectric layer is subjected to a longitudinal strain, $s_{long}$. The radius of curvature can be found by [65]:

$$\frac{1}{r} = \frac{2\left|s_{long}\right|(t_p + t_e)(A_p E_p A_e E_e)}{4(E_p I_p + E_e I_e)(A_p E_p + A_e E_e) + (A_p E_p A_e E_e)(t_p + t_e)^2} \tag{2.3}$$

where $A_p$ and $A_e$ are the cross-sectional areas of the piezoelectric and the elastic layer, $E_p$ and $E_e$ are the Young's modulus of the piezoelectric and the elastic layer, and $t_p$ and $t_e$ are the thickness of the piezoelectric and the elastic layer. Fig. 2.16 shows an schematic drawing of a MEMS scanner based on piezoelectric actuators [11]. A fabricated device [12] based on piezoelectric actuators is shown in Fig. 2.17.

The first piezoelectric thin-film actuated scanner was developed in 2005 [66]. One significant drawback of piezoelectric actuation is the limited stroke length of the actuator. To solve this problem, Baran [13] proposed a novel actuation scheme with a mechanically coupled indirect drive. As shown in Fig. 2.18, once actuated, since the mass of the mirror plate is much smaller than the actuated section, the motion of the mirror plate is therefore enlarged. An alternative to piezoelectric film is the use of piezoelectric bulk elements [67]. Using a stacked piezoelectric actuator, the rotation angle is improved without losing the resonance frequency.

One unique performance characteristic of magnetic actuation over electrostatic, thermal, and piezoelectric actuators is the ability to generate torque and achieve large angular displacement. Electromagnetic actuator takes the advantage of Lorentz force. These actuators usually comprise of an coil and permanent magnets (providing magnetic field). When current flows in the coil, Lorentz force is applied onto the coil, driving the mirror [68, 69]. The magnitude of the the

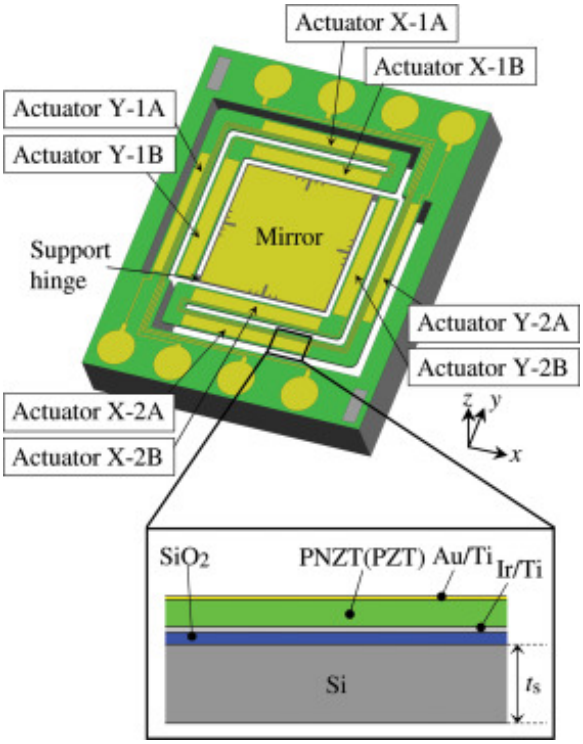


Figure 2.16: Schematic drawing of a piezoelectric MEMS scanner. Reprinted from [11]

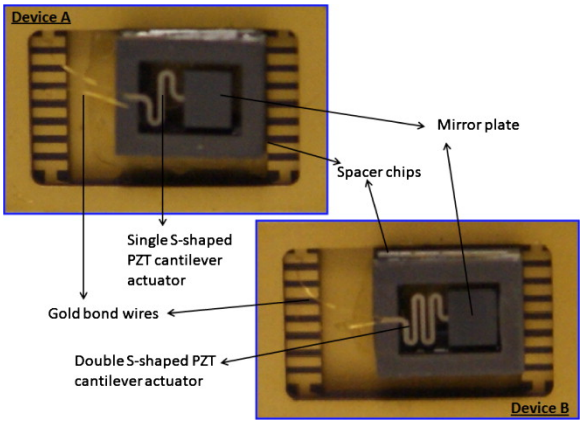


Figure 2.17: A fully assembled piezoelectric actuated MEMS mirror. Reprinted from [12]

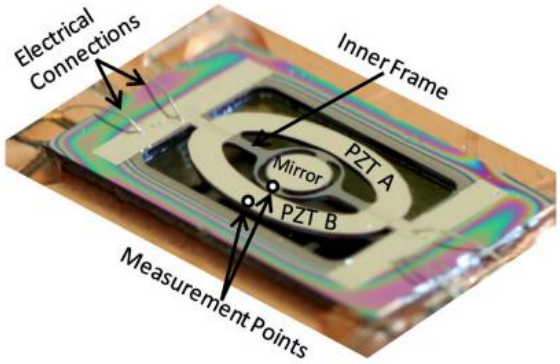


Figure 2.18: The structural layout of a piezoelectric micromirror with coupled indirect driving. Reprinted from [13]

magnetic torque at a given displacement angle $\theta$ is approximated as [70]:

$$M_{mag} = M_s V_{magnet} H_1 cos(\theta) \tag{2.4}$$

where $M_s$ is the internal magnetization, $V_{magnet}$ is the volume of the magnet, and $H_1$ is the magnetic field intensity. The angular displacement is related to the magnetic torque according to,

$$\theta_{max} = \frac{M_{mag} l}{EI} \tag{2.5}$$

$l$ is the cantilever length, $E$ is the Young's Modulus, and $I$ is the momentum is inertia of the cantilever. By solving the two equations above, the magnitude of the magnetic torque and the angular displacement can be found:

$$y_{max} = \frac{M_{mag} l^2}{2EI} \tag{2.6}$$

Fig. 2.19 shows picture of the MEMS scanners actuated by electromagnetic actuators [14]. With a novel design integrating the torsional hinges with the actuation coils [15], the scanning angle can be increased (Fig. 2.20).

Bulk silicon micromachining [71] and surface micromachining [16] are both used to fabricate electromagnetic actuated micromirrors. The tilting angle is primarily restricted by the coil current

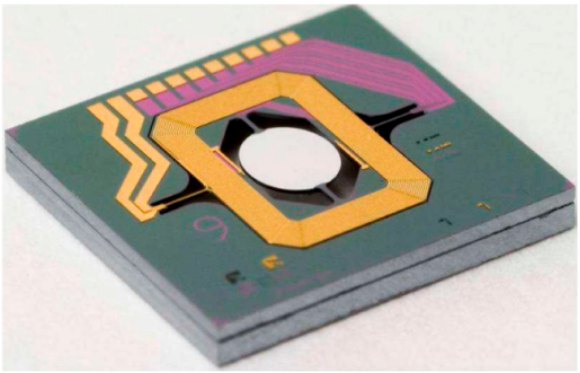

Figure 2.19: A fully assembled electromagnetic actuated MEMS mirror. Reprinted from [14]

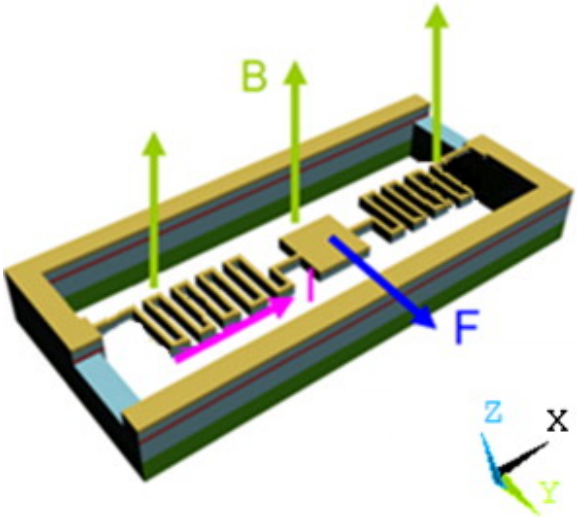


Figure 2.20: An electromagnetic MEMS scanner integrating the coil with torsional hinges. Reprinted from [15]

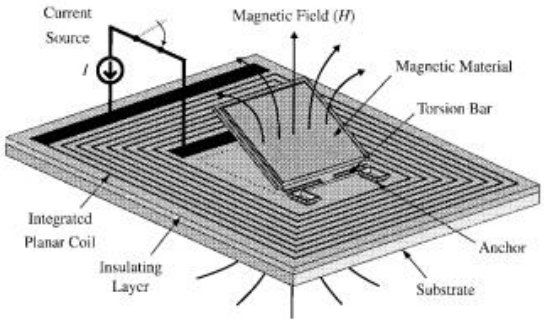


Figure 2.21: A schematic representation of a torsional structure actuated by the magnetic field generated by an inductor coil. Reprinted from [16]

of an external electromagnet. Permalloy coatings provide better angular resolution (Fig. 2.21). At first, two single axis electromagnetic MEMS mirror were cascaded [72]. An early two-axis electromagnetic scanner was fabricated by bulk micromachining [73] with relatively low field of view even at resonance frequency. Ahn and Kim [74] shows improved performance for MEMS electromagnetic two-axis mirror. A layer of BCB, silicon nitride and aluminum forms the torsion suspensions and serves as multi-level interconnect for independent control of the electromagnetic coils. Hybriding two motion modes is reported by Bourounia [75, 17]. By employing magnetostrictive effect, remotely actuated two-axis scanning can be achieved. In this work, bending and twisting motion are simultaneously excited in a cantilevered mirror (Fig. 2.22). A piezoresistive sensor is included to form a close loop for feedback control. A combination of electrostatic and electromagnetic two-axis scanner has become popular recently [76, 18]. As shown in Fig. 2.23, slow-axis is driven by electromagnetic actuator for the outer frame and fast-axis is electrostatically actuated in the inner frame. Slow-axis and fast-axis torsional hinges are orthogonal to each other.

Since MEMS micromachining techniques largely evolve from integrated circuit (IC) fabrication, silicon has historically dominated MEMS systems. However, the majority of such silicon--based MEMS devices suffer from silicon's poor fracture toughness and fatigue behavior [77]. Based on different applications and stress requirements, different materials have been studied to replace silicon as hinges in MEMS devices. For example, metal and metal alloys have been fab-

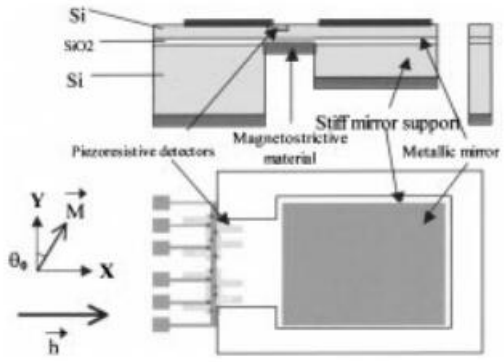


Figure 2.22: A schematic drawing of magnetostrictive actuation. Reprinted from [17]

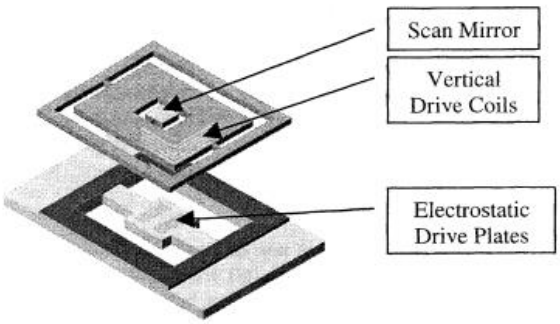


Figure 2.23: A twoaxis scanning mirror hybriding electrostatic and electromagnetic driving mechanism. Reprinted from [18]

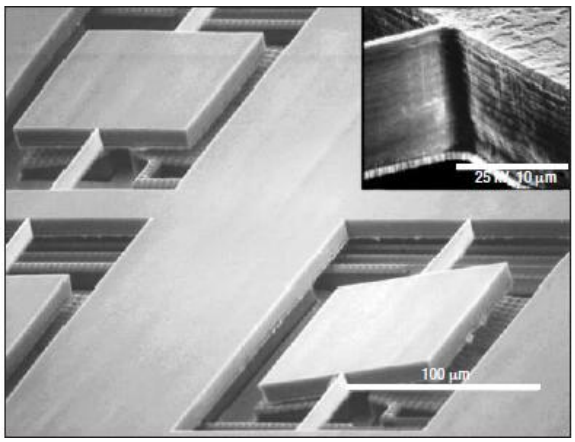


Figure 2.24: Microfabricated titanium mirror array. Reprinted from [19]

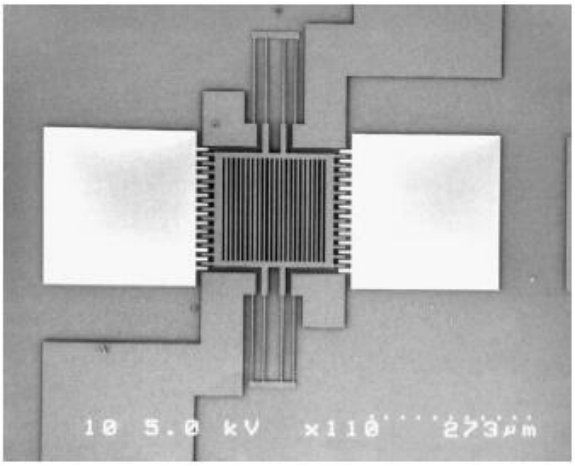


Figure 2.25: SEM of 3C–SiC beams patterned using RIE. Reprinted from [20]

ricated into MEMS hinges [19] to provide higher fracture resistivity. Compatible with traditional reactive ion etching process, the aspect ratio in metal and metal alloy device is not lost (Fig. 2.24). In order to overcome harsh environment and high frictional forces, ceramic [20] and diamond films [78] are micromachined (Fig. 2.26). To further increase the scanning field of view, traditional silicon flexures are replaced by more flexible carbon fiber flexures [21]. This device (Fig. 2.26) is actuated with an external piezo drive that makes very large scan angles possible.

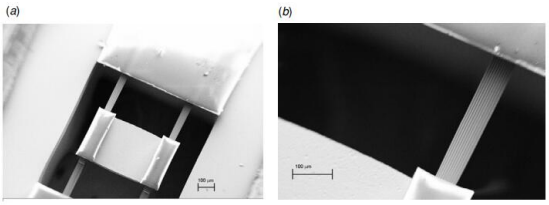


Figure 2.26: The structural layout of a piezoelectric micromirror with coupled indirect driving. Reprinted from [21]

## 2.3 Previous Work

From actuation perspective, most current MEMS scanning mirrors are not suitable for under water operations. Electrostatic actuated MEMS mirrors suffer from electric shorting problem in water. Excessive cooling effect in water hinders thermoelectric actuators from effective operations. A major drawback of piezoelectric actuators is the short stroke length [79, 80]. Some sort of leverage is needed for relatively large scan angles but the effectiveness of leverage is questionable in water due to fluidic damping. In the past few years, water-immersible MEMS scanning mirrors have undergone active development [81, 82]. In both prototypes, electromagnetic actuators were chosen because these electromagnetic actuators were not sensitive to environment. Huang [81] used 5 inductor coils and 2 pairs of permanent magnets to drive two modules: fast-axis module and slow-axis module.

In term of the torsional hinges, silicon hinges are easy to be fabricated and the process is compatible with traditional IC fabrication procedures. However, they are not suitable for under water operations since they are not resistive to impacts. Metal and metal alloy, ceramic and diamond have even higher shear modulus [83], therefore, not suitable for underwater operation. Carbon fibers have lower shear modulus, and thus providing large scanning field of view without losing their mechanical property. However, established fabrication processes include bonding carbon fibers into substrate trenches manually. The performance consistency and batch fabrication capability become questionable. In [81], a polymer material is proposed to be fabricated into torsional hinges, ensuring a reliable performance in water. The torsional hinges were fabricated from biaxially-oriented

polyethylene terephthalate (BoPET) film with laser micromachining. BoPET film proved to be a good candidate for water-immersible operations because its moderate shear modulus. It is much smaller than silicon, making BoPET hinges resistive to shocking and liquid damping. Meanwhile, the shear modulus is neither too small, ensuring the resonant frequency of these BoPET hinges sensitive to their geometric shapes. The theoretical analysis of the resonant frequency of torsional hinges will be discussed in Section 3. These BoPET torsional hinges provided repeatable and reliable under water performances. In the prototype of Kim [82], polydimethylsiloxane (PDMS) was used to fabricate torsional hinges. Similar to BoPET, these PDMS torsional hinges are resistive to strong damping of torsional oscillation by water. An advantage over BoPET is that PDMS-based soft lithography process has a higher resolution than laser micromachining. It is possible to fabricate small torsional hinges, reducing the overall package size.

An obvious drawback of these scanning mirrors is the package size. Compared with traditional MEMS scanning mirrors, these centimeter level scanners are too bulky to be integrated into handheld probes. One reason lies in the electromagnetic actuators. In both prototypes, x-direction and y-direction scanning were actuated independently: at least four inductor coils were employed. Therefore, even the scanning part can be fabricated in a very compact fashion, it is hard to reduce the size of the actuators. Another reason is the torsional hinge material. Admittedly, PDMS is suitable to operate in water. One drawback is that the shear modulus is too low. In raster scanning, the scanning frequency of one direction (fast-axis) has to be a lot higher than the other direction (slow-axis). To realize this, the slow-axis torsional hinge has to be slender, occupying a lot space on the mirror plate. The situation is better for BoPET since its shear modulus is significantly higher than PDMS. But due to the high chemical stability of BoPET, high-resolution patterning still poses a challenge.

# 3. IMPROVING RELIABILITY OF TWO-AXIS WATER-IMMERSIBLE SCANNING MIRROR THROUGH STRUCTURAL DESIGN*

## 3.1 Introduction

In this chapter, the development of a two-axis water-immersible scanning is presented. The fast-axis of this mirror is able to reach a mechanical scanning angle of $\pm 15^{\circ}$ at the resonant frequency of 320 Hz in air, and $\pm 12.5^{\circ}$ at the resonant frequency of 230 Hz in water, respectively. The slow-axis is able to reach a mechanical scanning angle of $\pm 15^{\circ}$ at the resonant frequency of 24 Hz in air, and $\pm 12.5^{\circ}$ at the resonant frequency of 13 Hz in water, respectively. The two scanning axes have very different resonance frequencies, which are suitable for raster scanning.

First, a previously published prototype scanning mirror is discussed. The advantages and disadvantages are analyzed. To overcome the drawbacks of this prototype, a new design that brings fast-axis and slow-axis torsional hinges to the same plane is proposed. The theoretical relationship between the torsional hinges and their resonant frequencies is included. Second, prototype device is fabricated and tested. Deep ion reactive etching (DRIE) and laser micromachining processes have been developed. The characterization result shows predictable, stable and repeatable scanning pattern in both air and water. At last, B-mode images acquired by this scanning mirror have been presented to verify its capability in ultrasound/photoacoustic imaging systems.

As is discussed in Chapter 1, Dr. Huang presented a water-immersible scanning mirror prototype [81]. This mirror is a inspiring starting point for future devices for the following reasons: (1) electromagnetic actuator is suitable for under water applications; (2) BoPET has a lower shear modulus, minimizing the chance of shocking damage and required driving force. However, several issues still exist in its design and fabrication, which hinders its practical applications. As shown in

*Reprinted with permission from "A microfabricated water-immersible scanning mirror with a small form factor for handheld ultrasound and photoacoustic microscopy." by Song Xu, Chih-Hsien Huang, and Jun Zou, 2016. MOEMS and Miniaturized Systems XV, Vol. 9760, p. 976002, Copyright [2016] by International Society for Optics and Photonics.

Fig. 3.1, the scanning mirror consists of two independent modules for two-axis scanning, respectively. The fast-axis scanning module is directly mounted onto the slow-axis module. Fast-axis module is driven by one inductor coil and slow-axis module is driven by another four. First, a total of five inductor coils makes this prototype bulky. Second, once both axes actuated, the entire fast-axis module, including mirror plate, fast-axis anchor, permanent magnets and inductor coil, is in motion. The connection wire supplying power to the fast-axis inductor coil is dangling, devastating the module reliability and scanning pattern predictability. Third, it should be noticed that fast-axis torsional hinge is not on the same plane of slow-axis torsional hinge. Consequently, the fast-axis scanning pattern is located on an arc. Therefore, if coupled with a focused transducer, the resolution is lost. To address the above issues, a newly designed water-immersible two-axis MEMS scanning mirror is developed.

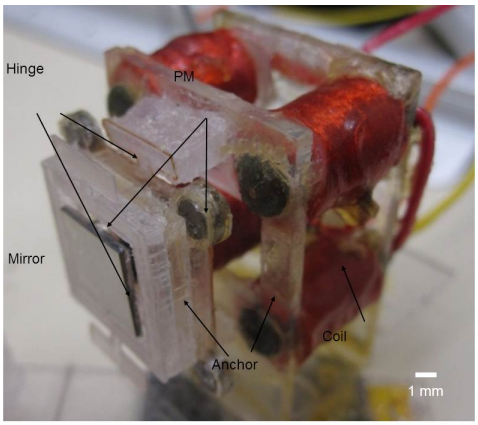


Figure 3.1: A fully assembled prototype of water-immersible scanning mirror.

## 3.2 Design

Fig. 3.2 shows the schematic top and side view of the new water-immersible two-axis scanning mirror, respectively. It consists of an aluminum coated silicon mirror plate to provide excellent optical and acoustic reflectivity. The silicon mirror plate is supported on the supporting hinge by two flexible BoPET torsional hinges, which form the fast scanning axes. The entire assembly is

supported on the outer supporting hinge by another two flexible BoPET torsional hinges with lower force constant, which form the slow axes. An acrylic spacer is attached to the bottom of the outer supporting hinge to create space for mirror plate torsion. The two torsional hinges are made of BoPET films. The low stiffness and high fracture strain of the BoPET material help to reduce the required driving force and minimize the chance of shock damage in water.

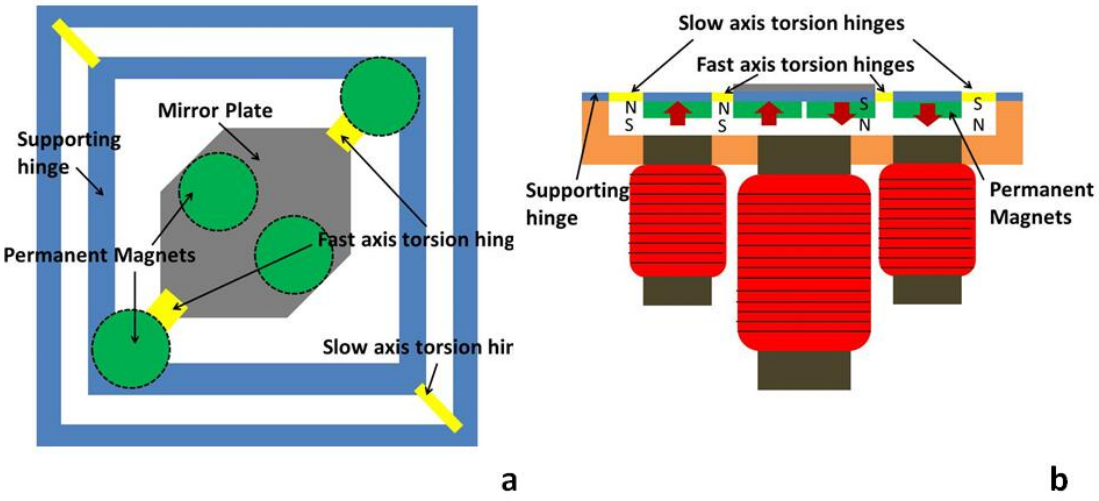


Figure 3.2: Schematic view of the two-axis water-immersible scanning mirror: (a) top-view; (b) side-view.

Electromagnetic actuation is chosen as the driving mechanism to enable reliable underwater scanning because of its low power requirement. Compact electromagnetic actuation is achieved by combining a single inductor coil with two rare-earth magnet discs attached onto the two ends of the mirror plate with opposite polarities. When an AC or DC current flows through the inductor coil, the resultant magnetic field creates a torque on the magnets and thus rotates the mirror around the torsional supporting hinges. Three inductor coils and four rare-earth magnet discs are arranged into two groups to provide torques for the two scanning axes. Due to the heavier scanning mass and also softer supporting hinges, the resonant frequency of the slow-axis is much lower than that of the fast-axis.

| | fast-axis | slow-axis |
|---|---|---|
| hinge length (L) | 0.2 mm | 1.4 mm |
| hinge width (b) | 1.2 mm | 0.5 mm |
| hinge thickness (h) | 0.2 mm | 0.2 mm |
| magnetic disc distance (d) | 5.1 mm | 18.4 mm |
| | module dimensions | |
| length | 16 mm | |
| width | 16 mm | |
| height | 13 mm | |
| BoPET shear modulus | 0.12 GPa | |

Table 3.1: Main design parameters of the water-immersible two-axis scanning mirror.

The main design parameters of this two-axis scanning mirror are listed in Table 3.1. Given geometry shape and size of torsional hinges, resonant frequencies can be calculated and actual hinge sizes can be determined. According to [84], the governing equation for the torsional oscillations is

$$GK\frac{\partial^2\Phi(x,t)}{\partial x^2} - \rho_c I_p \frac{\partial^2\Phi(x,t)}{\partial t^2} = M(x,t) \tag{3.1}$$

where $G$ is the shear modulus, $K$ is a geometric function of the cross section of the beam, $\rho_c$ is cantilever density, $I_p$ is the polar moment of inertia. For a thin rectangular beam in this case,

$$K = bh^3/3,\ I_p = b^3h/12 \tag{3.2}$$

$\Phi(x,t)$ is the deflection angle about the major axis of the cantilever, $M(x,t)$ is the applied torque per unit length along the beam and $x$ is the spatial coordinate along the length of the beam and $t$ is time. [84] provides boundary conditions

$$\Phi(0,t) = \frac{\partial\Phi(x,t)}{\partial x}\Big|_{x=L} = 0 \tag{3.3}$$

and solution of Eq. 1:

$$\omega_{water}^{(n)} = \omega_{air}^{(n)}\left[1 + \frac{3\pi\rho b}{2\rho_c h}\Gamma_t(n)\right]^{-1/2} \tag{3.4}$$

where $\omega_{water}^{(n)}$ is n-th order resonant frequency in water, $\omega_{air}^{(n)}$ is n-th order resonant frequency in vacuum, $\rho$ is fluid density and $\Gamma_t(n)$ is the hydrodynamic function for torsional oscillations. $\Gamma_t(n)$ can be approximated by Pade approximants:

$$\Gamma_t(\kappa) = \frac{1}{16}\left(\frac{1 + 0.37922\kappa + 0.072912\kappa^2}{1 + 0.37922\kappa + 0.088056\kappa^2 + 0.010737\kappa^3}\right) \tag{3.5}$$

$\kappa$ is normalized mode number

$$\kappa = \frac{\pi}{2}(2n-1)\frac{b}{L}. \tag{3.6}$$

Air resonant frequency ($\omega_{air}^{(n)}$) is determined by material property and its geometric shape only:

$$\omega_{air}^{(n)} = \frac{D_n}{L}\sqrt{\frac{GK}{\rho_c I_p}}, D_n = \frac{\pi}{2}(2n-1). \tag{3.7}$$

In our case, only first order resonant (n=1) is considered. The estimated resonant frequencies of the scanning mirror in both air and water are listed in Table 3.2.

| | fast-axis | slow-axis |
|---|---|---|
| $\omega_{vac}^{(1)}$ | 369 Hz | 39 Hz |
| $\omega_{fluid}^{(1)}$ | 277 Hz | 20 Hz |

Table 3.2: Estimated resonance frequencies.

### 3.3 Fabrication

The fabrication of the miniaturized water-immersible scanning mirror was conducted as follows. First, the reflective mirror ($6 \times 8\ mm^2$), and the supporting hinge were etched out from a polished single-crystalline silicon substrate by reactive-ion etching (RIE)(Fig. 3.3(a)). The polished silicon substrate provides excellent surface smoothness and flatness, and also good acoustic reflectivity due to the large acoustic impedance mismatch between silicon ($19.6 \times 10^6\ Ns/m^3$) and water ($1.47 \times 10^6\ Ns/m^3$). A thin layer of aluminum coating ($70\ nm$) was deposited onto

the silicon mirror surface using e-beam evaporation to enhance its optical reflectivity. Second, the BoPET torsional hinges (Fig. 3.3(b)) and acrylic frames (Fig. 3.3(c) and (d)) were made by using a laser cutting machine. During the assembly, the silicon mirror plate and the inner supporting hinge were first bonded on the BoPET torsional hinge (Fig. 3.4(a)). Then this part was attached to the outer supporting hinge from the top (Fig. 3.4(b)). The permanent magnet discs (D21B-N52, K&j Magnetics) and the acrylic spacer 1 was bonded from the bottom (Fig. 3.4(c)). Lastly, the inductor coils (70F103AI-RC, BOURNS and 70F331AF-RC, BOURNS) and the acrylic spacer 2 were assembled and bonded together (Fig. 3.4(d)). Silicon rubber adhesive (RTV 108, Momentive Performance Materials) was used as the bonding agency. After insulating the coils and electrical connections, this water-immersible twoaxis scanning mirror could be immersed in water to ensure reliable underwater scanning operation (Fig. 3.5).

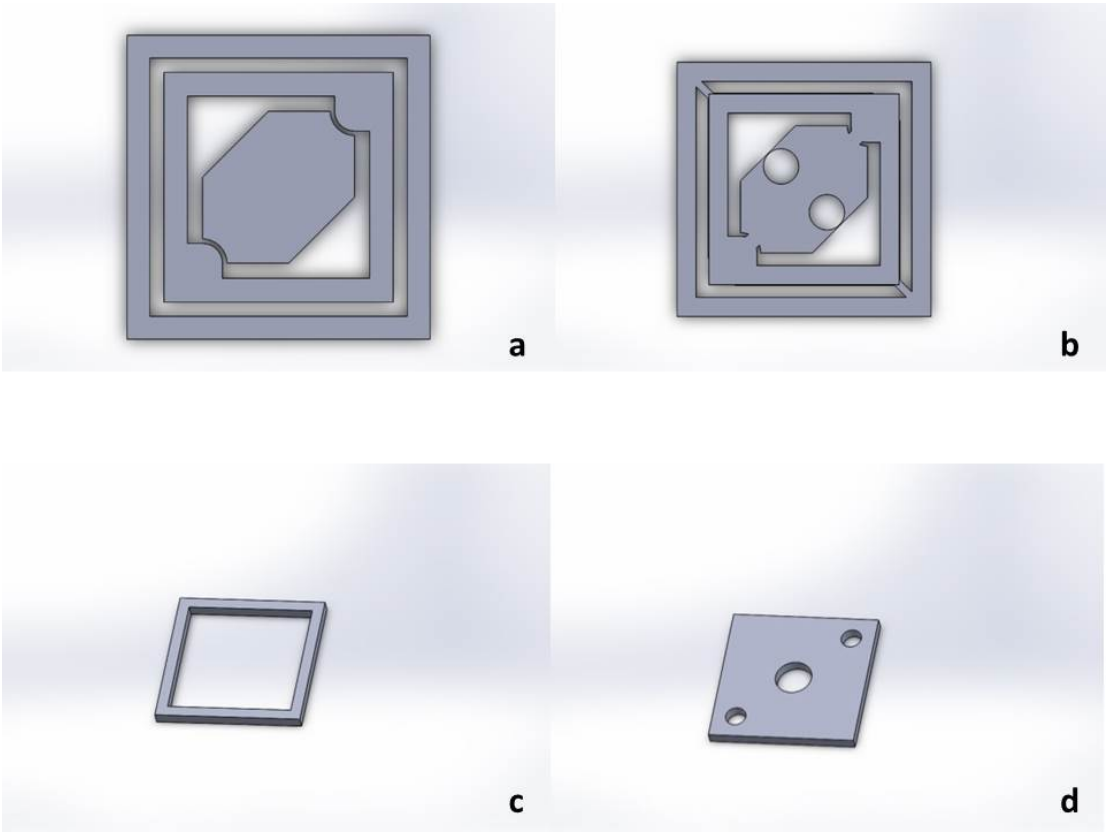


Figure 3.3: Prepared parts of the mirror: (a) mirror plate and supporting hinge; (b) BoPET torsional hinges; (c) acrylic spacer 1; and (d) acrylic spacer 2.

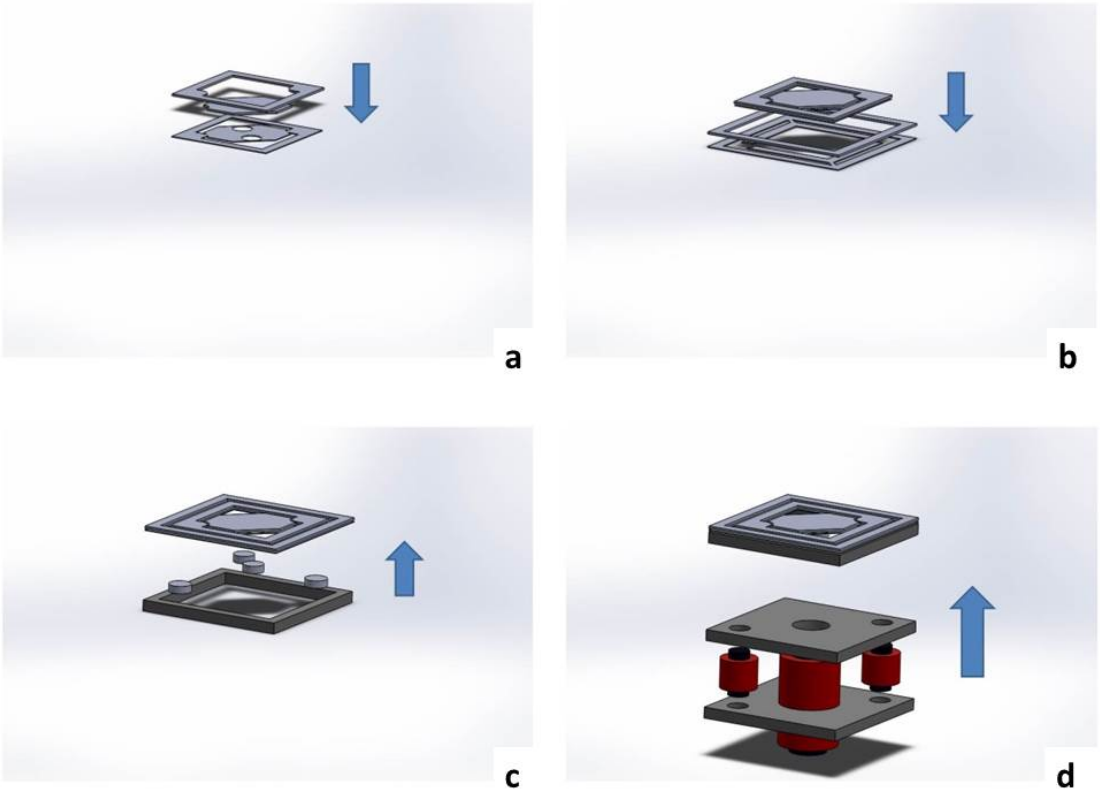


Figure 3.4: Assembly process: (a)mirror plate and inner supporting hinge; (b) outer supporting hinge; (c) permanent magnets and acrylic spacer 1; and (d) inductor coils and acrylic spacer 2.

### 3.4 Scanning Characterization

The scanning performance is characterized by a laser tracing method (Fig. 3.6). This two-axis mirror is fixed in a water tank at 45 degrees to horizontal. Laser is projected onto the center of the mirror plate and reflected vertically to horizontal. A ruler placed 60 mm from the center of the mirror plate shows the mirror scanning path. The scanning angle is calculated based on the trace of the laser beam on the ruler. To determine the resonance frequency, AC driving currents with the same amplitude but different frequencies are applied. The resonance frequency is defined as the frequency at which the AC driving current when the scanning angle reaches its maximum. As shown in Fig. 3.7, in air, fast-axis resonance frequency is determined to be 320 Hz and in water, 230 Hz. For slow-axis, a resonance frequency of 13 Hz in water and 24 Hz in air can be

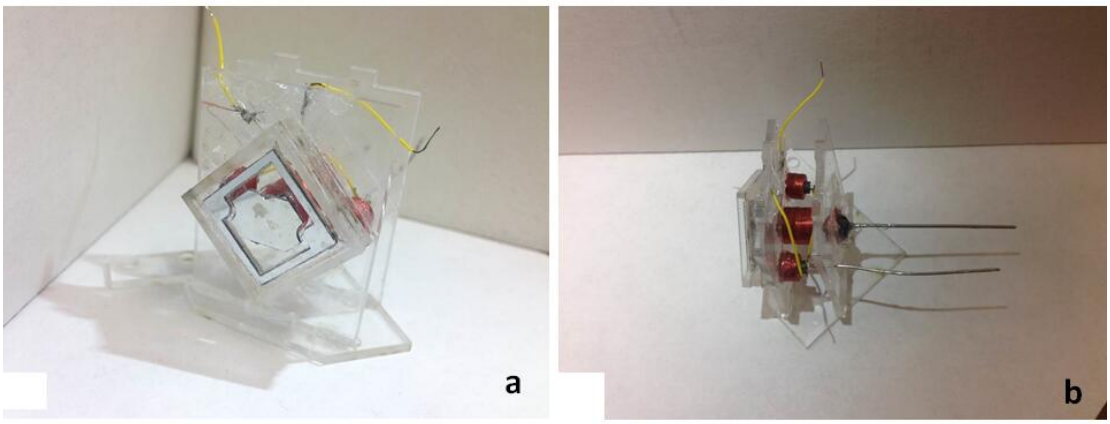


Figure 3.5: Assembled prototype: (a) front-view; and (b) side-view.

achieved. As the driving current increases linearly, the scanning angle also increases in a linear fashion (Fig. 3.8). To justify the decoupling between the two axes, a raster scanning result is demonstrated (Fig. 3.9). Both fast-axis and slow-axis are driven in their resonance frequencies and their phase synchronized. In addition, fast axis was kept running at 230 Hz, 100 mA in water and slow axis was kept running at 60 mA, 13 Hz in water for over 10 million cycles as a reliability test. No noticeable degradation in scanning performance was found. Based on these characterization results, this mirror module has met design requirements and is ready for ultrasound imaging tests.

### 3.5 Ultrasound Imaging Experiment

Utilizing miniaturized two-axis water-immersible scanning mirror to steer focused ultrasound beam in water, we could demonstrate B-mode images. By stacking these B-mode images, a 3D image could be reconstructed. The imaging setup included a water tank, a 25 MHz focused transducer (V324-Su, Olympus) with a focal length of 50.8 mm, water-immersible scanning mirror and three 0.9 mm pencil leads as targets. These three pencil leads were arranged in parallel at 2 mm interval to $30^\circ$ to horizontal. The scanning mirror is placed 25.4 mm away from transducer at an angle of 45 degrees. Targets are placed 25.4 mm from scanning mirror such that these three targets are located in the focal zone. The ultrasound transducer is connected to a pulser/receiver system (5072PR, Olympus). The pulse repetition rate is 5 kHz. An amplifier is used to provide AC

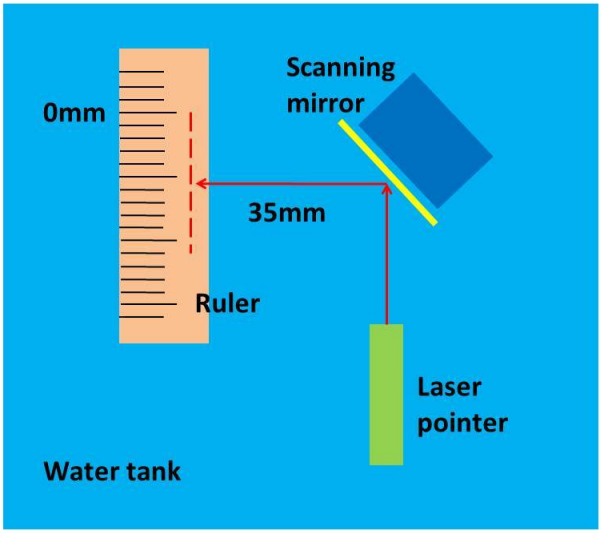


Figure 3.6: Laser tracing method.

current to drive the scanning mirror. In order to balance scanning field of view and pixel density, fast-axis is driven at 100 Hz, 150 mA; slow-axis is driven at 1 Hz, 100 mA. A LabView (National Instruments) program is developed to control the DAQ card. Fig. 3.10(a) shows B-scan result. By stacking 20 B-mode images along slow-axis scanning direction, a 3D image can be generated (Fig. 3.10(b)). At -6dB, the target width is determined to be 967 $\mu$m, which is close to the actual target size.

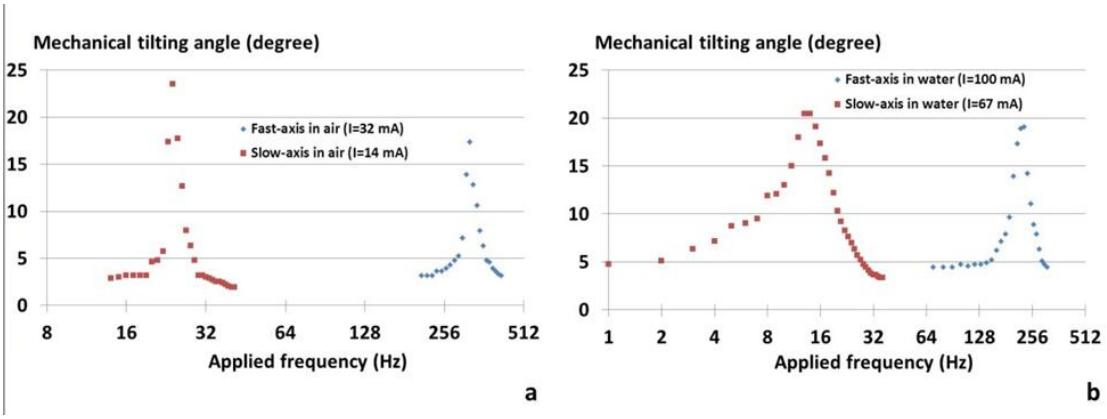


Figure 3.7: Resonant frequencies of the two-axis scanning mirror: (a) results in air; and (b) results in water.

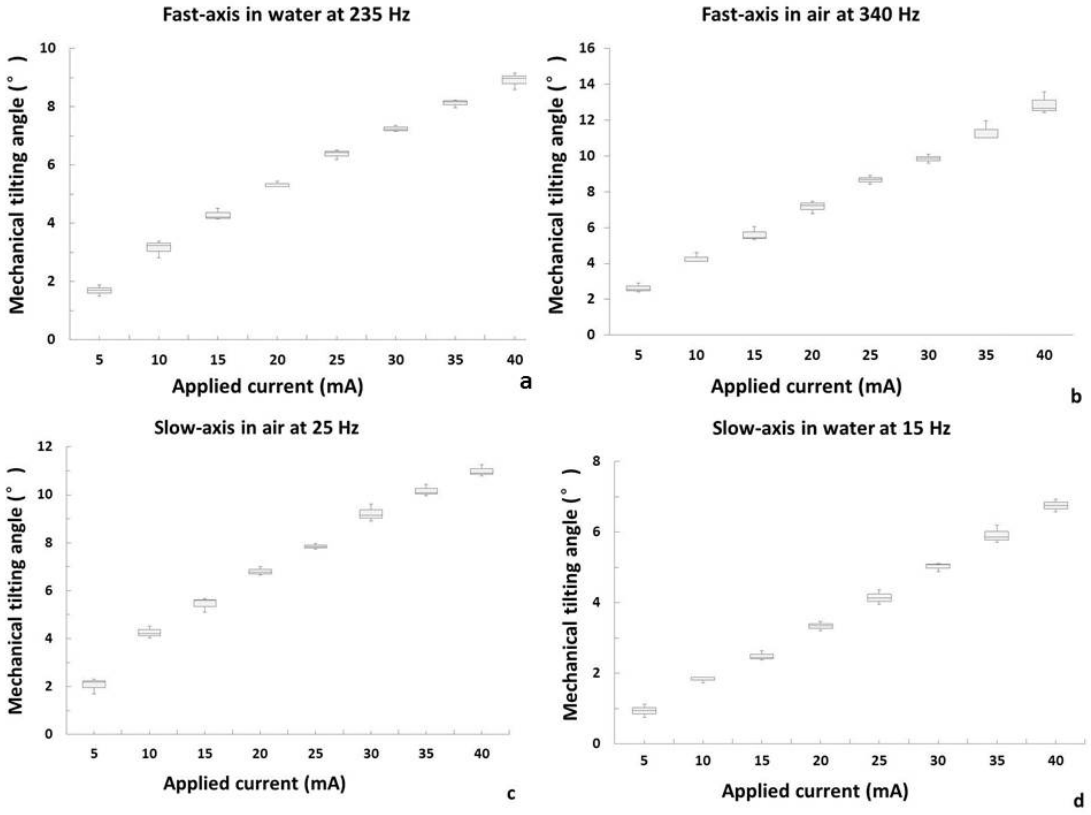


Figure 3.8: The scanning angle increases linearly with the driving current amplitude.

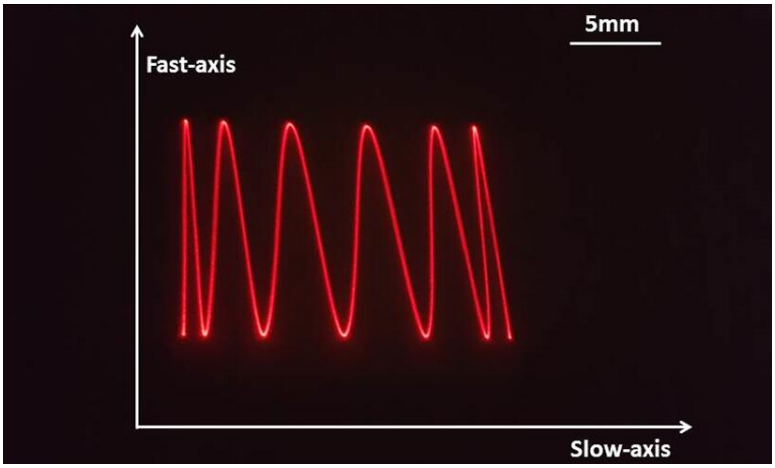


Figure 3.9: Raster scanning result of the two-axis water-immersible scanning mirror.

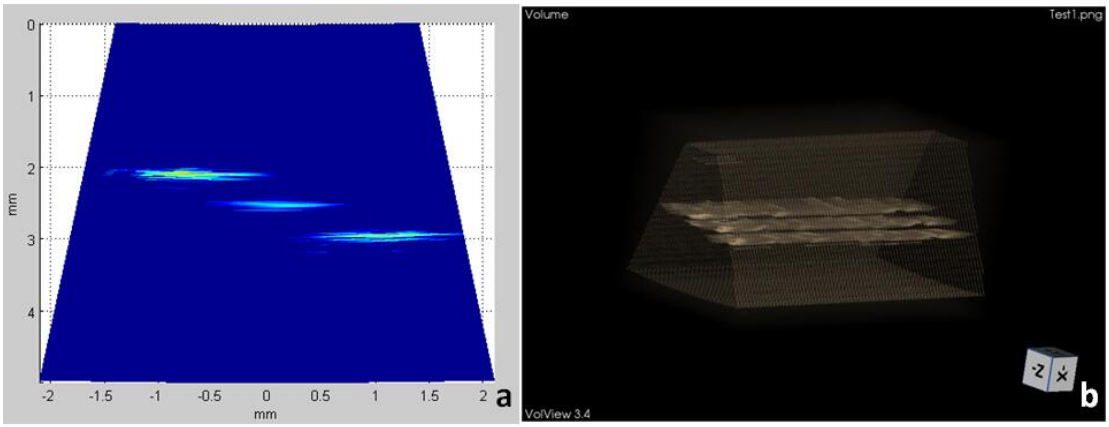


Figure 3.10: Ultrasound test results: (a) B-mode slice of the target cross section; and (b) 3D image by stacking 20 slices of B-image.

# 4. MINIATURIZATION OF SINGLE-AXIS WATER-IMMERSIBLE SCANNING MIRROR THROUGH STRUCTURAL IMPROVEMENT*

## 4.1 Introduction

Compared with traditional MEMS scanners, the overall size of the prototype discussed in Chapter 2 is too large, hindering its practical applications in handheld probes. One approach to smaller size is to re-evaluate the old design. In this chapter, a new single-axis water-immersible scanning mirror with a small form factor is presented. Electromagnetic actuation method and torsional hinges fabricated from BoPET film are inherited from previous prototype. One improvement this mirror targeting is to shrink the overall package size without losing much of the mirror plate size, which determines the numerical aperture. To realize this, a new layout embedding the torsional hinge underneath the mirror plate is proposed. A $7 \times 5\ mm^2$ mirror plate serves as the optical/ultrasound reflector on a $7 \times 5 \times 7\ mm^3$ package, covering the entire surface area. It can achieve one-axis scanning of $\pm 12.1^\circ$ at a resonant frequency of 250Hz in air and 210Hz in water, respectively. The small form factor, large scanning angle, and high resonant frequency of the new water-immersible scanning mirror make it suitable for building compact handheld imaging probes for *in vivo* high-speed and wide-field ultrasound and photoacoustic microscopy.

## 4.2 Design

Fig. 4.1 shows the schematic design of the single-axis water-immersible scanning mirror. Similar with last prototype, a single crystal silicon substrate coated with a thin aluminum layer is used as the reflective mirror plate. Silicon has much higher acoustic impedance than water and therefore provides high acoustic reflectivity, while the aluminum coating forms a good optical reflection layer. The mirror plate has a rectangular shape to better fit the oval optical/ultrasound illumination

*Reprinted with permission from "Two-axis water-immersible microscanning mirror for scanning optics and acoustic microscopy." by Song Xu, and Jun Zou, 2016. Journal of Micro/Nanolithography, MEMS, and MOEMS, Vol. 15, p. 045005, Copyright [2016] by International Society for Optics and Photonics.

spot. Two pairs of permanent magnets provides torques to drive the mirror: the left two magnets are polarized in one direction whereas the right two are polarized in another direction. A spacer frame creates space for the magnets once actuated. The BoPET film layer is attached to the spacer frame from the bottom. Underneath the BoPET film lies a cap structure. Two torsional hinges (yellow in Fig. 4.1) connect the cap structure with the spacer frame. An inductor coil (housed in mounting structure) is fixed to the cap structure to provide magnetic field. When a current flows through the inductor coil, a resultant magnetic field creates attractive force on one pair of magnets; meanwhile repulsive force on the other pair. Since the mounting structure, inductor coil and the cap structure are fixed, the mirror plate, spacer frame are actuated around the torsional hinges, realizing single-axis scanning.

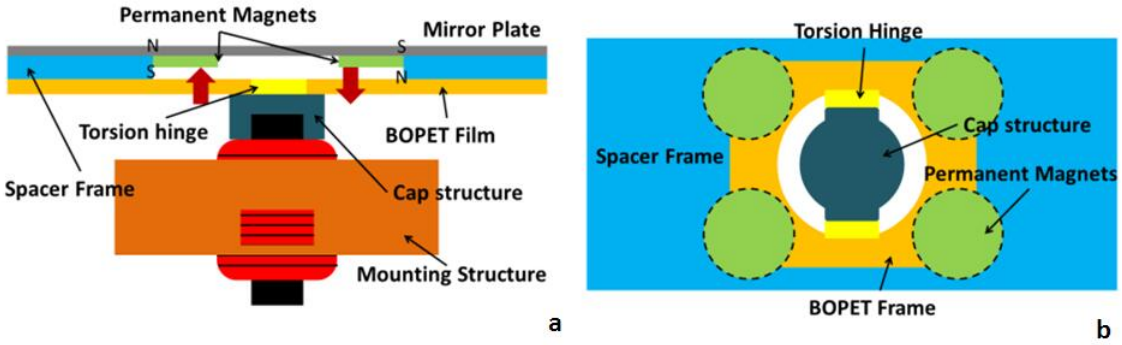


Figure 4.1: Schematic design of the single-axis mirror: (a) side-view; and (b) top-view.

To achieve significant reduction of the overall size, improvements are made over the design discussed in Chapter 2. First, instead of been placed adjacent to the mirror plate, the two torsional hinges are completely removed from the surface and relocated underneath the mirror plate. Therefore, the mirror plate can occupy all the surface area. Second, the inductor coil, together with the cap structure, is used as the supporting structure, reducing the height of the module. Third, in this mirror, we use four magnets instead of two to provide stronger and more uniform magnetic field, which allows the use of a smaller inductor coil to drive the mirror. In ultrasound and photoacoustic

microscopy, the optical and ultrasound signals are in the form of short pulses with a typical repetition rate of 10~100 kHz. To maintain a dense pixel formation, the vibration frequency of the scanning mirror should be 10 to 100 s of Hz. A maximal scanning angle larger than $10^{\circ}$ is desirable to provide a good field of view. The main design parameters of the scanning mirror are listed in Table 4.1. Based on these design parameters, following a similar calculation discussed in Chapter 2 [84], a preliminary mechanical analysis was conducted to provide a first-order estimation of the resonant frequency. The estimated resonant frequencies of the scanning mirror in air and water are 263 Hz and 215 Hz, respectively.

| Inductor | | Permanent Magnets | |
|---|---|---|---|
| inductance | 1 mH | thickness | 0.8 mm |
| | | diameter | 3.125 mm |
| | | spacing | 3 mm×4 mm |
| Mirror Plate | | Supporting Hinge | |
| length | 7 mm | length | 0.75 mm |
| width | 5 mm | width | 5 mm |
| thickness | 0.3 mm | thickness | 0.3 mm |

Table 4.1: Main design parameters of the single-axis water-immersible two-axis scanning mirror.

### 4.3 Fabrication and Assembly

The fabrication of the scanning mirror started with the preparation of the reflective mirror plate. A $300\ \mu m$ thick single-crystalline silicon wafer was coated with $150\ nm$ thick aluminum layer by using electron-beam evaporation (PVD 75 Ebeam Evaporator, Lesker). After this, it was cut into multiple 7 mm $\times$ 5 mm pieces by using an automatic dicing machine (1006A, Micro Automation), which will be used as the reflective mirror plate. The torsion hinges, spacer frame and inductor cap were made by using a laser cutting machine (PLS6.75, Universal Laser System). The torsion hinges were cut out from a $75\ \mu m$ thick BOPEF film, and the spacer frame and inductor cap were cut out from a 1 mm thick acrylic sheet. Because of its complex 3D shape, the inductor housing

(with two mounting holes inside) were fabricated by using a high-resolution optical 3D printer ($Perfactory^{®}$ Micro DDP, Envisiontec) with a maximal resolution of $30\ \mu m$.

After all the components were fabricated, the silicon mirror plate was first bonded to the spacer frame. Permanent magnetic discs (D101-N52, K&J Magnetics) were fixed inside the spacer frame. BoPET film was bonded to the spacer frame. hinges were first assembled and bonded together with silicone rubber adhesive (RTV 108, Momentive Performance Materials) (Fig. 4.2(a)). Second, one end of the magnetic core of the inductor coil (70F103AI-RC, BOURNS) was polished into a flat surface, followed by the mounting and bonding of the inductor cap (Fig. 4.2(b)). Next, the inner ends of the two torsional hinges were bonded onto the inductor cap (Fig. 4.2(c)). In the last step, two electrical wires were connected to the inductor coil and insulated with silicone rubber adhesive (Fig. 4.2(d)). Fig. 4.3 shows a completely assembled scanning module. It has an overall length, width, and thickness of 7 mm, 5 mm and 7 mm, respectively, which is much smaller than our previous scanning mirror module without losing much of the mirror plate size.

## 4.4 Characterization

The scanning angle and resonance frequency of the scanning mirror were characterized in air and water by using a laser tracing method. During the characterization, the scanning mirror was mounted on the bottom of a water tank. A ruler was placed at 35 mm away from the center of the mirror plate. The laser beam from a laser pointer was projected onto the mirror plate with an incident angle of $45^{\circ}$ and reflected onto the ruler. The scanning angle was calculated based on the trace of the laser beam on the ruler. To determine the resonance frequency, AC driving currents with the same amplitude but different frequencies were applied. The resonance frequency is defined as the frequency of the AC driving current when the scanning angle reaches its maximum.

Fig. 4.4 shows the scanning angles at different frequencies both in air and in water. The amplitude of the AC driving currents is 90 mA in air and 97 mA in water, respectively. Due to the dynamic damping in water, the resonance frequency drops from 250 Hz in air to 210 Hz in water, which are close to the estimated values. Fig. 4.5 shows the average values and standard deviations of the optical tilting angles (based on five measurements) as a function of the amplitude

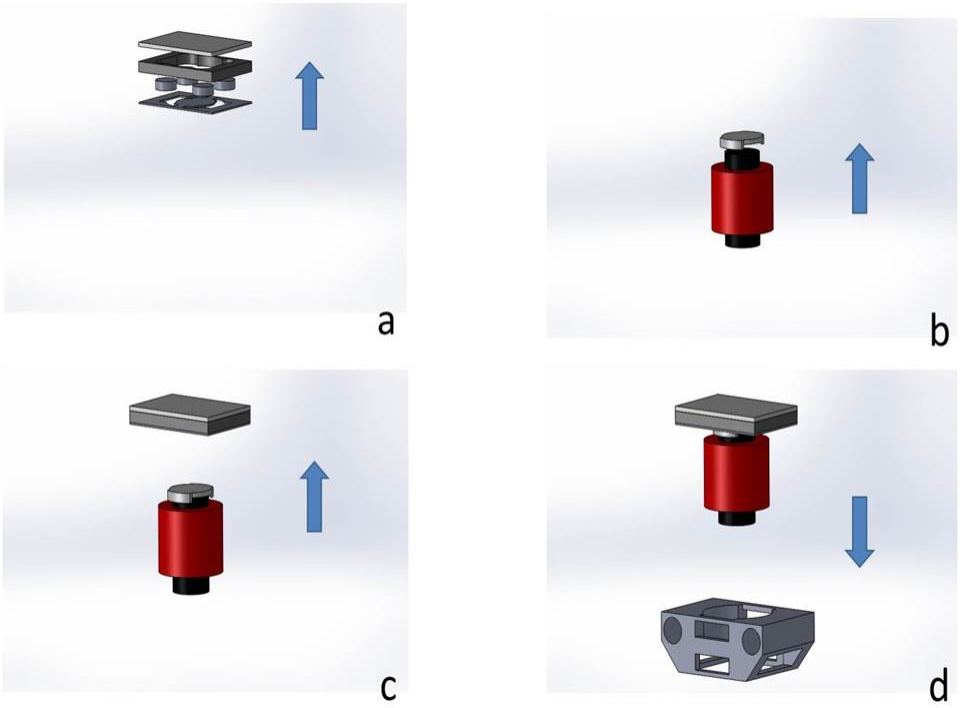


Figure 4.2: Single-axis scanning mirror assembly procedure: (a) mirror plate, magnets, spacer frame and BoPET film were first bonded; (b) cap structure was bonded to the inductor coil; (c) cap structure was fixed to the BoPET film from the bottom; (d) inductor coil was housed in the mounting structure.

of the AC currents when the scanning mirror was driven at its resonant frequency in air and water, respectively. In water, as the current increasing from 20 mA to 120 mA, optical tilting angle increase linearly from $4^\circ$ to $12.5^\circ$. On the other hand, as current decreasing from 120 mA to 20 mA, the linearity can also be observed. In air, at low current, optical tilting angle also varies linearly with respect to AC current. However, at high current, linearity is distorted a little because the tilting angle is so large that BoPET hinge can no longer hold its mechanical property. Since tilting angles required in ultrasound and photoacoustic scanning are usually smaller than nonlinear region values, it is safe to draw a conclusion that optical tilting angle increases linearly with the amplitude of the AC driving currents.

In addition, a thermal conductivity and reliability test was also performed when the scanning mirror was immersed in water at $25^\circ C$. A thermal couple probe was put in direct touch with

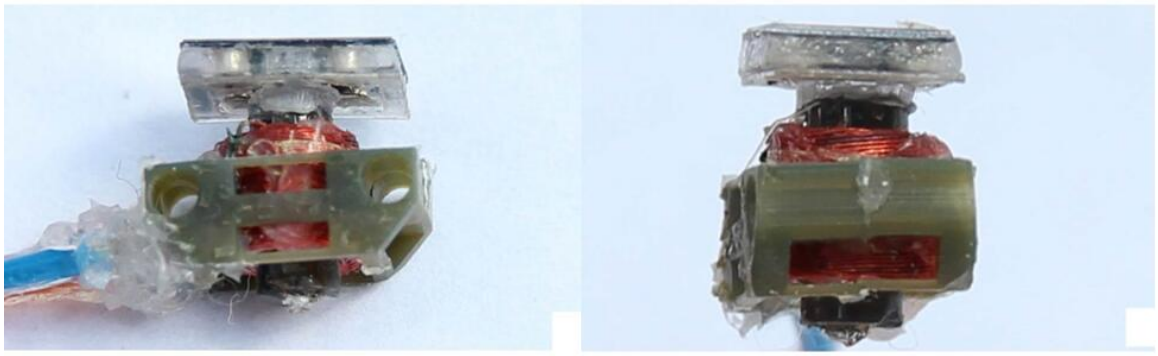

Figure 4.3: Fully assembled prototype.

inductor coil to monitor the change of its temperature. The scanning mirror was driven at 210 Hz with an AC current of 230 mA. The temperature of the inductor coil stayed constantly at $31°C$. After being driven over 10 million cycles, no noticeable degradation in the scanning performance was observed.

### 4.5 Ultrasound Imaging Experiment

Using the water-immersible scanning mirror to steer focused ultrasound beam in water, pulse-echo ultrasound microscopy of an optical-fiber target were successfully demonstrated. The imaging setup includes a water tank, a high-frequency (25 MHz) focused transducer with a focal length of 50.4 mm (V324-SM-F2.00IN-PTF, Olympus), the water-immersible scanning mirror, and a piece of 0.9 mm pencil lead as the imaging target. The scanning mirror is placed 28 mm away from the transducer at an angle of $45°$. The pencil lead is placed 32 mm away from the center of the mirror plate, such that they are located in the focal zone of the ultrasound transducer. The ultrasound transducer is connected to a pulser/receiver system (5072PR, Olympus) and an oscilloscope (TDX 2014B, Tektronix). The pulses repetition rate and pulse width were set to be 5 kHz and $1\mu s$, respectively. A DAQ card (PCI 6251, National Instruments) and a custom-built current amplifier array were used to provide DC currents to drive the scanning mirror from -350 to 350 mA with a 7 mA increment. This forms 100 scanning steps, corresponding to a scanning area of 3 mm. The peak-to-peak voltage of the received ultrasound signals were measured and averaged 128 times.

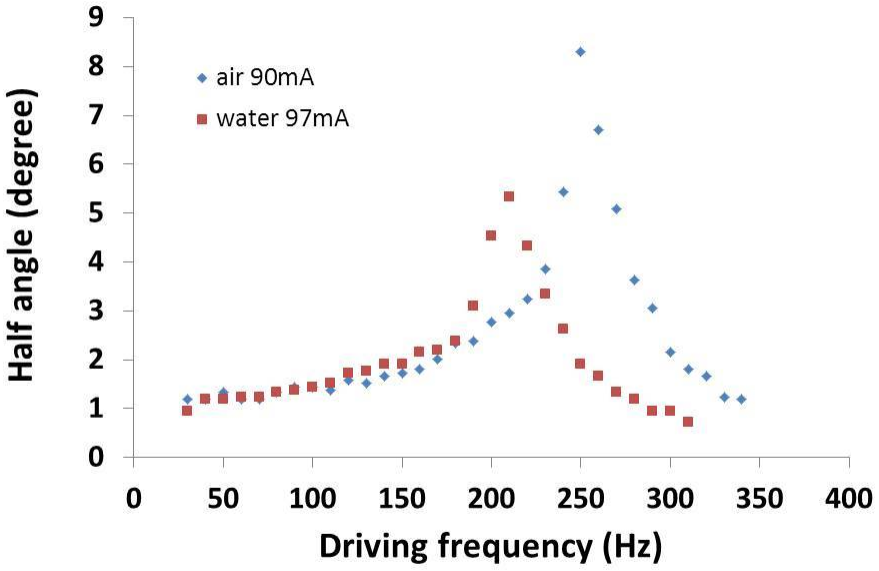


Figure 4.4: Resonant frequency characterization in air and water.

To automate the scanning and data acquisition process, a Labview (National Instruments) program was developed to control the DAQ card and the oscilloscope. Fig. 4.6 shows the normalized averaged peak-to-peak voltages as a function of the lateral and vertical scanning location. The target width is 1.08 mm in ultrasound image, which agreed well with the actual pencil lead width. There are two hot spots in ultrasound image. One illustrates upper water-target interface and the other one illustrates bottom target-water interface. Space between these two surfaces denotes the target.

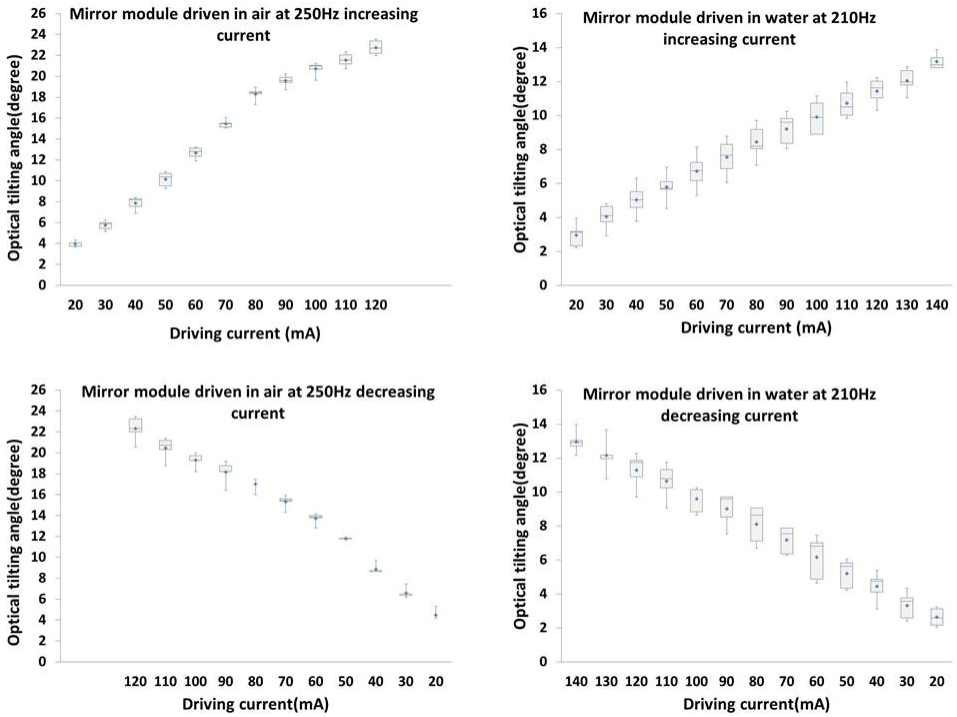


Figure 4.5: Scanning angle characterization in air and water.

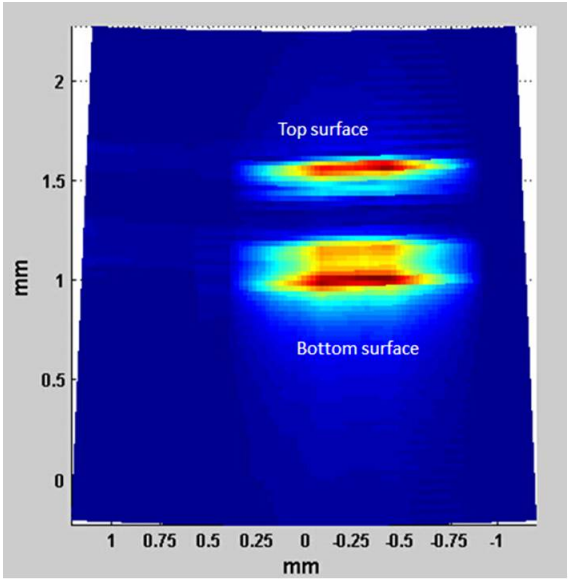


Figure 4.6: B-mode image of a 1-mm target.

# 5. MINIATURIZATION OF TWO-AXIS WATER-IMMERSIBLE SCANNING MIRROR THROUGH NOVEL ACTUATION MECHANISM*

## 5.1 Introduction

Combining both rich optical contrast and deep acoustic penetration depth beyond optical diffraction limit, photoacoustics has emerged as a new hybrid bio-imaging modality [85, 86]. As discussed in previous sections, flexible polymer torsional hinges and electromagnetic actuators proved to be reliable components fabricating MEMS scanning mirrors reflecting both optical and ultrasound signals. However, to enable two-axis scanning, multiple off-chip inductor coils are needed. As a result, the entire scanning mirror package could be very bulky. This situation makes it difficult to build compact photoacoustic probes for *in-vivo* imaging applications.

To address this issue, a new electromagnetic two-axis water-immersible scanning mirror driven by only one inductor coil is reported and its ultrasound scanning capability in 3D ultrasound microscopy demonstrated. This is made possible by taking advantage of the different resonance frequencies of the two scanning axes to suppress their mechanical coupling via intrinsic dynamic structural filtering [87, 88]. Independent control of two scanning motions can be achieved without using multiple inductor coils. In addition, a new data acquisition and image reconstruction strategy is also developed to improve the density of the data points and the spatial resolution of the ultrasound image. This approach opens a new possibility for miniaturizing the electromagnetic two-axis micro water-immersible scanning mirrors. It can also be used for the development of other types of multi-axis electromagnetic micro actuators with a small form factor.

*Reprinted with permission from "A Two-Axis Water-Immersible Micro Scanning Mirror Driven by Single Inductor Coil through Dynamic Structural Filtering." by Song Xu, Xiaoyu Duan, and Jun Zou, 2018. Sensors and Actuators A: Physical, Vol. 284, p. 172–180, Copyright [2018] by Elsevier.

## 5.2 Operation Principle

Fig. 5.1a shows the schematic top view of the electromagnetic two-axis water-immersible scanning mirror. The dashed line and arrows indicate the location and direction of the side-view shown in Fig. 5.1b. It consists of a relective mirror plate, an inner and outer frame, two pairs of torsional hinges, four permanent magnets, and one inductor coil. One pair of permanent magnets (with opposite magnetization) is attached to the bottom of the mirror plate. The other pair (also with opposite magnetization) is attached to the inner frame. When a current is flowing through the inductor coil, the generated magnetic torque rotates the mirror plate and inner frame around their supporting hinges, which provides fast- and slow-axis scanning, respectively (Fig. 5.1c).

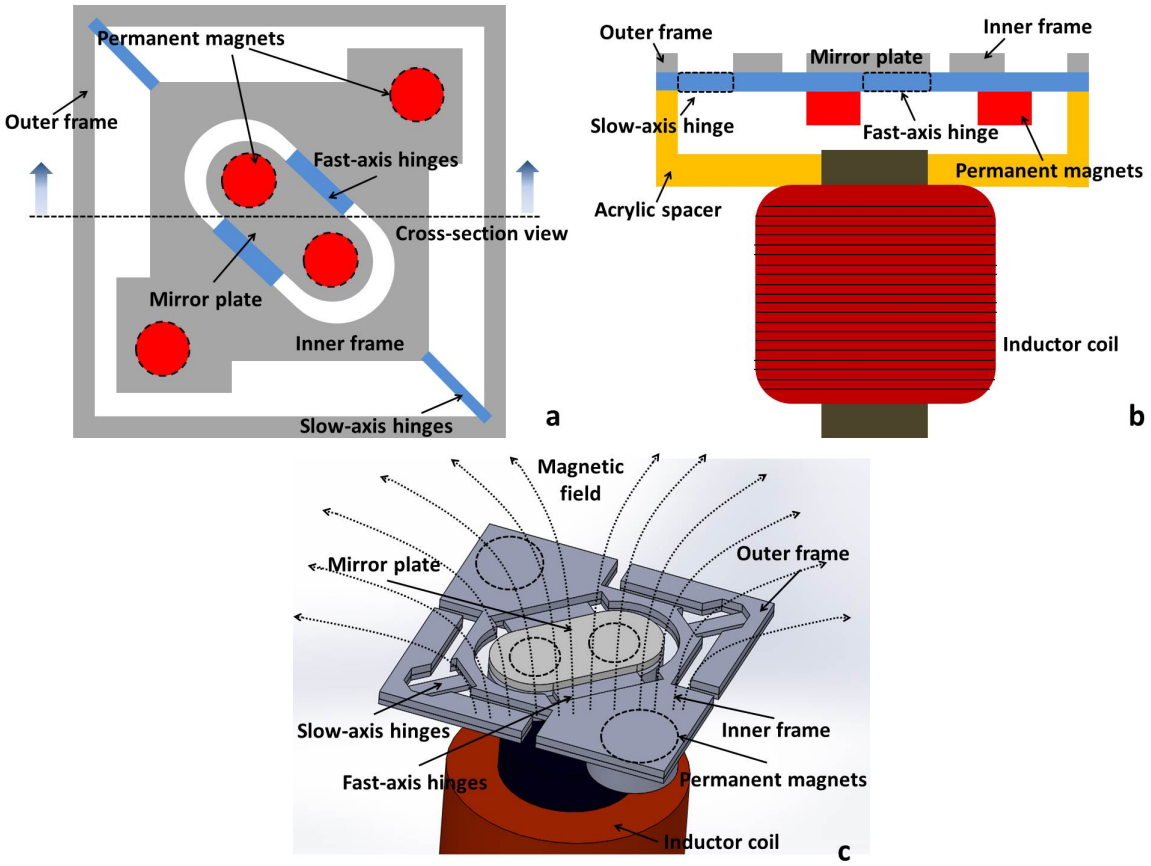


Figure 5.1: Schematic design of the two-axis water-immersible scanning mirror: (a) top view; (b) cross-section view; (c) 3D view.

To enable the dynamic structural filtering, the resonance frequency of fast-axis ($\omega_{r\_f}$) should be much higher than that of slow-axis ($\omega_{r\_s}$). The driving sensitivity of the slow-axis should be higher than that of fast-axis, such that the slow-axis can be driven by a smaller current (Fig. 5.2). The above two requirements can be easily met by tuning the torsional spring constant and moment of inertia of both fast and slow axes. When an AC current with two resonance frequency components ($I(t) = I_f sin(\omega_{r\_f}t) + I_s sin(\omega_{r\_s}t), I_s < I_f$) is applied onto the inductor coil, the resulting scanning angles of the fast and slow scanning axes can be determined by:

$$O_f(t) = I_f A_{r\_f} sin(\omega_{r\_f}t) + I_s A_{0\_s} sin(\omega_{r\_s}t) \tag{5.1}$$

$$O_s(t) = I_f A_{\infty\_f} sin(\omega_{r\_f}t) + I_s A_{r\_s} sin(\omega_{r\_s}t) \tag{5.2}$$

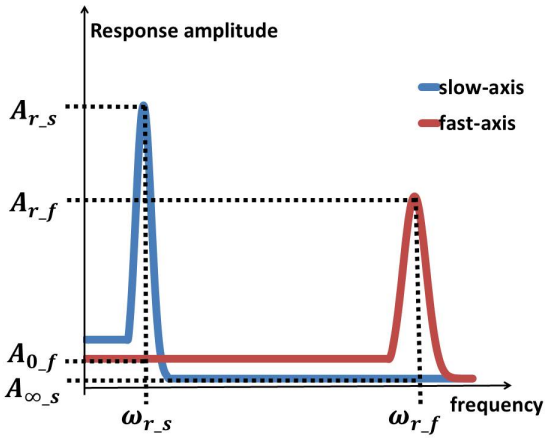


Figure 5.2: Desirable dynamic response of the fast- and slow-axis.

Since $I_s A_{0\_s}$ is much smaller than $I_f A_{r\_f}$, it will be largely suppressed. The scanning angle of the fast-axis is deminated by:

$$O_f(t) = I_f A_{r\_f} sin(\omega_{r\_f}t) \tag{5.3}$$

Similarly, since $\omega_{r\_s} << \omega_{r\_f}$, $I_f A_{\infty\_f}$ will be very small. The scanning angle of the slow-axis

is determined by:

$$O_s(t) = I_s A_{r\_s} sin(\omega_{r\_s} t) \tag{5.4}$$

Therefore, the scanning motions of the fast- and slow-axis are decoupled and can be independently controlled. In addition, with both scanning axes driven at their resonance frequencies, minimal driving current is needed to reach certain scanning angle, resulting in a most power-efficient driving condition.

### 5.3 Design and Fabrication

A prototype two-axis scanning mirror with single inductor coil was designed, fabricated and tested. The main design parameters are listed in Table 5.1. Based on the geometric and mechanical parameters of the BoPET hinges, the scanning resonance frequencies were estimated in $COMSOLMultiphysics^{®}$ (Fig. 5.3). The bulk viscosity parameter was taken into account to simulate both air- and water-immersed vibrations. The dynamic behavior of the modeled micro scanning mirror was dominated by the first eigenmodes. In air, the resonance frequencies of the fast and slow axes were estimated to be 750 Hz and 74 Hz, respectively. In water, the resonance frequencies of the fast and slow axes were estimated to be 658 Hz and 63 Hz, respectively. To calculate the quality factor, the driving frequency was swept $\pm 10$ Hz around the resonance frequency to determine the tilting angle of the mirror plate (Fig. 5.4).The quality factors were then calculated (as the ratio between resonance frequency and the full width at half maximum) to be $Q_{fast\_air} = 375.4$, $Q_{slow\_air} = 37.8$, $Q_{fast\_water} = 164.5$, and $Q_{slow\_water} = 31.5$.

The mirror fabrication and assembly process is shown in Fig. 5.5. As shown in Fig. 5.5a, the mirror plate, inner frame and outer frame were etched out as an entire piece from a 300--$\mu m$-thick single-side polished silicon wafer with deep reactive ion etching (DRIE). Small linker structures were used to connect the mirror plate, inner frame and outer frame in one piece to facilitate following fabrication steps. After assembly, these liners were removed with a razor blade. The torsional hinge plates were cut from a 130-$\mu m$-thick BoPET film by using a $CO_2$ laser cutter.

| | Fast-axis | Slow-axis |
|---|---|---|
| Hinge length ($L$) | 0.05 $mm$ | 1.5 $mm$ |
| Hinge width ($b$) | 4.5 $mm$ | 1 $mm$ |
| Permanent magnet distance ($2r$) | 5 $mm$ | 10 $mm$ |
| Rotational mirror plate size (x $\times$ y) | 4 $mm \times 8$ $mm$ | 8 $mm \times 5$ $mm$ |
| | BoPET film | |
| Shear modulus ($G$) | 0.02 $GPa$[89] | |
| Density ($\rho_c$) | 1.455 $g/cm^3$[89] | |
| | Inductor coil | |
| Inductance | 33 $mH$ | |
| Coil length | 15 $mm$ | |
| Coil diameter | 8 $mm$ | |
| | Permanent magnet | |
| Diameter | 3.0 $mm$ | |
| Height | 0.7 $mm$ | |
| Density | 7.5 $g/cm^3$ | |
| | Viscosity[90] | |
| Water | 1.002 $mPa - s$ | |
| Air | 18.6 $\mu Pa - s$ | |

Table 5.1: Main design parameters of two-axis micro scanning mirror driven by single actuator.

Four through holes were also cut to serve as a template for assembling the permanent magnets. Two acrylic spacers were also cut from a 1.5-$mm$-thick acrylic plate with the $CO_2$ laser cutter. To improve the alignment accuracy, small holes with 100-$\mu m$ diameter (not shown in Fig. 5.5a) were etched on the silicon pieces (including mirror plate, inner and outer frames) and also formed onto the BoPET hinge plate and acrylic spacers to serve as the alignment marks for their assembly.

For mirror assembly, water-proof silicone rubber adhesive (RTV 108, Momentive Performance Materials) was used as the bonding agent. The silicon pieces, the BoPET hinges plate and the spacer #1 were first bonded together (Fig. 5.5b). Several section of 100-$\mu m$ optical fiber were inserted into the alignment holes to mechanically align them together. Two pairs of magnetic discs (D101-N52, K&J Magnetics) were bonded onto the bottom surface of the mirror plate and inner frame, respectively (Fig. 5.5c). Lastly, the inductor coil was attached to the acrylic spacer #2 and bonded with the assembled top structure (Fig. 5.5d). The fully assembled prototype scanning mirror (10 $\times$ 10 $\times$ 15 $mm^3$, 28 g) is shown in Fig. 5.5e. It should be noted that the edges of

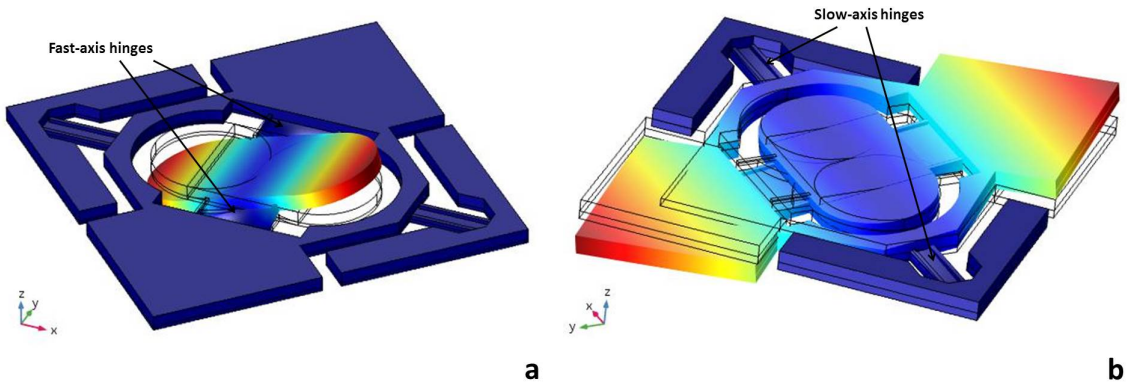


Figure 5.3: Simulated mirror plate tilting around: (a) the fast-axis and (b) the slow-axis. The edges of the BoPET hinges are broadened (with a thickness of 9.3 $\mu m$ and width of 11.4 $\mu m$) to better simulate their actual cross-section profile after laser cutting.

the torsional hinges are smooth after laser cutting. They appear coarse in the picture due to a small amount of silicone glue residue left after the assembly, which however should not affect the stiffness of the BoPET hinges. This is because the shear modulus of this silicon glue is much smaller than that of BoPET. After passivating the the inductor with a thin layer of epoxy (Epotek 301), the fabricated prototype scanning mirror is ready for testing in both air and water. Since the alignment marks on BoPET film and acrylic spacers were formed with laser cutting, the alignment accuracy is limited by the laser cutting resolution. When the size of the mirror is further reduced, new fabrication process with higher spatial resolution and alignment accuracy would be required.

## 5.4 Scanning Characterization

A laser tracing method was used to characterize the scanning performance of the two-axis single actuator mirror in both air and water. A CW laser was projected on the center of the mirror plate at an incident angle of $45^\circ$ and reflected vertically onto a ruler placed at certain distance from the mirror plate. The optical tilting angle was calculated based on the length of the laser scanning trace on the ruler. The resonance frequencies of the fast and slow axes were determined to be 720 Hz and 72 Hz in air, respectively (Fig. 5.6)a. In water, they were reduced to 690 Hz and 55 Hz, respectively (Fig. 5.6)b. From Fig. 5.6, the quality factors were calculated to

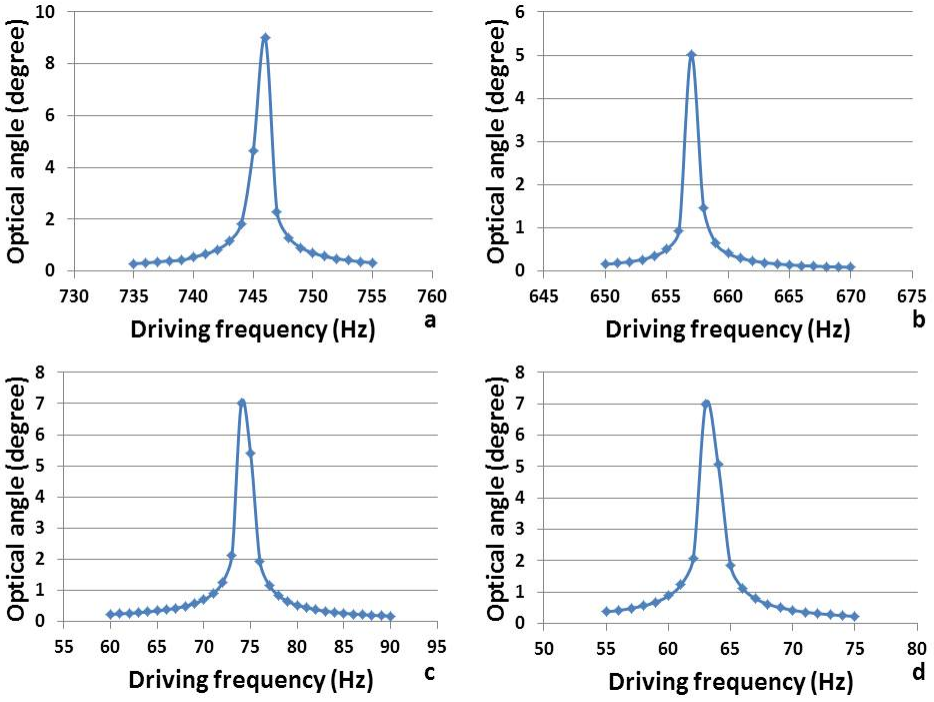


Figure 5.4: Simulation tilting angle of the mirror plate around (a) fast-axis in air; (b) fast-axis in water; (c) slow-axis in air; and (d) slow-axis in water.

be $Q_{fast\_air} = 13$, $Q_{slow\_air} = 25$, $Q_{fast\_water} = 9.8$, and $Q_{slow\_water} = 6.1$, which are much lower than the simulated values. This is because only viscous damping was considered in the simulation. In real testing , there were other damping sources, such as viscoelastic damping in the BoPET hinges and electromagnetic damping due to current induction in the inductor coil, which will further reduce the quality factors. The optical tilting angles of the fast and slow axes (at their resonance frequencies) driven by AC currents with different amplitudes were characterized (Fig. 5.7). The optical tilting angle increases almost linearly with respect to the current amplitude. An optical tilting angle of $\pm 10^{\circ}$ was achieved in air (with 2 mA for slow-axis and 30 mA for fast-axis) and in water (15 mA for slow-axis and 65 mA for fast-axis).

Raster scanning pattern with both axes actuated was also characterized (Fig. 5.8). The fast-axis was driven by a 28 mA current at 720 Hz, whereas the slow-axis was driven by a 2.8 mA AC current at 72 Hz. The two driving currents were synchronized and their phases were locked. Both axes have reached $\pm 9.5^{\circ}$ optical scanning angle. The resistance of the inductor coil is around $94\Omega$.

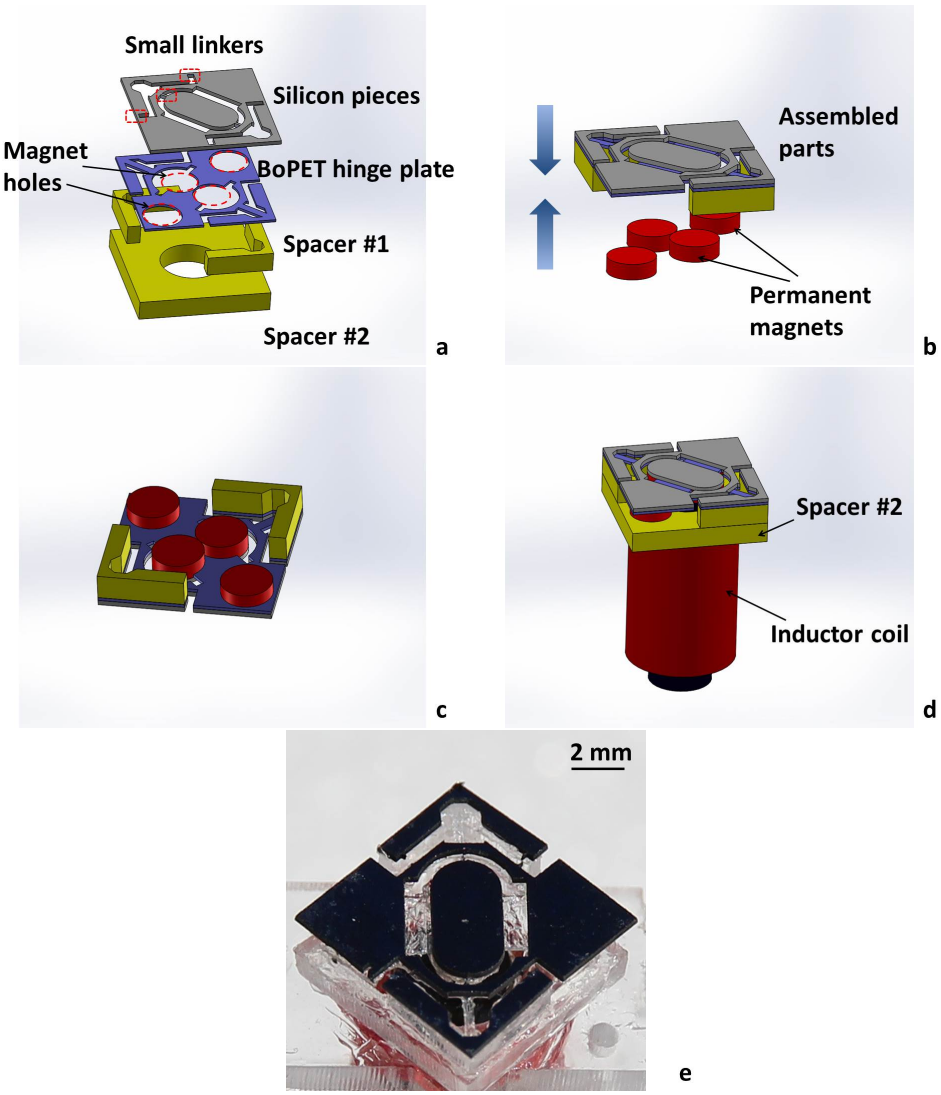


Figure 5.5: (a) through (d): fabrication and assembly process; (e) assembled prototype.

The power consumption of the scanning mirror is estimated to be 40 mW in air and 212 mW in water, respectively. Since the driving frequency of the fast-axis is 10 times of slow-axis, a half slow scanning cycle consists of 5 fast ones. It should be noted that in the raster scanning pattern, there is a slight vertical shift in the fast scanning cycles. This is because when the slow-axis is actuated, the orientation of the magnets around the fast-axis will be tilted, resulting in slight imbalance in the two electromagnetic forces between these two magnets and the inductor coil. However, as shown in Fig. 5.8, the raster scanning pattern is stable and repeatable. Therefore, once the scanning path

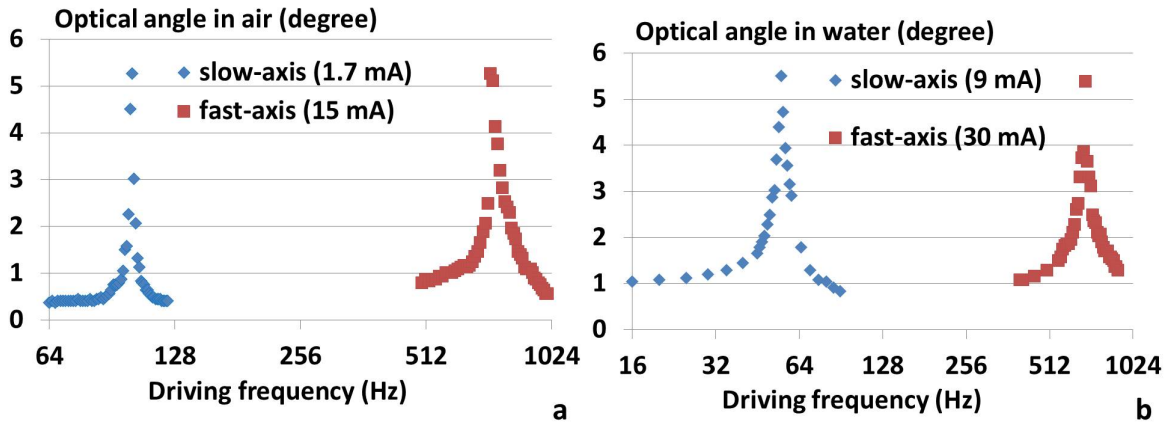


Figure 5.6: Resonance frequencies in (a) air and (b) water.

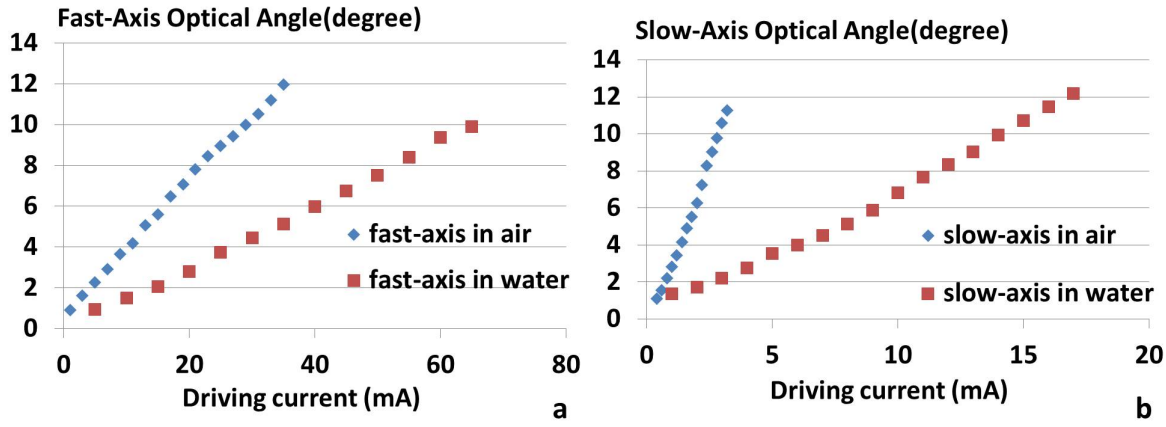


Figure 5.7: Optical scanning angle of (a) fast-axis and (b) slow-axis.

is calibrated, this shift should not be a big concern for retrieving the location of the scan points for image reconstruction purposes.

## 5.5 Ultrasound Imaging Setup and Data Acquisition

Fig. 5.9 shows the ultrasound microscopic imaging setup. The two-axis scanning mirror was immersed in water with the mirror plate facing downward at $45°$. An ultrasound transducer (V324--SM-F2.00IN-PTF, Olympus) was placed in water at 12 mm from the scanning mirror. It has a center frequency of 25 MHz and a focal length of 5 cm. A pulser/receiver (5072PR, Olympus) was connected to the transducer to send pulsed ultrasound signals to and receive the backscattered ones

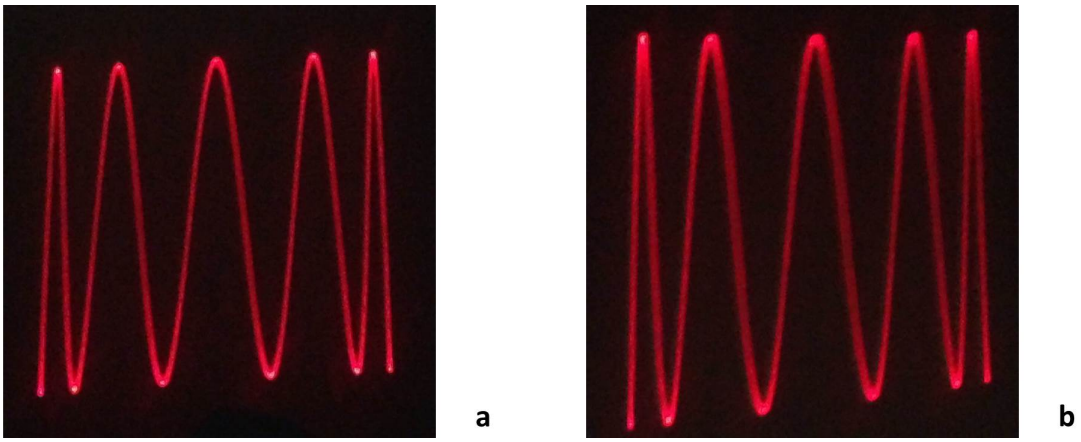


Figure 5.8: Raster scanning patterns in (a) air and (b) water.

("echoes") from the imaging target. The imaging target consisted of three 0.5-$mm$ tungsten wires, which were arranged on a $45°$ oblique plane with a pitch of 2 $mm$. The upper wire was placed at the focal point of the ultrasound transducer, which was located 39 $mm$ below the center of the mirror plate. The depth of focus of the transducer is around 3 $mm$. Therefore, all three tungsten wires are located inside the focal zone.

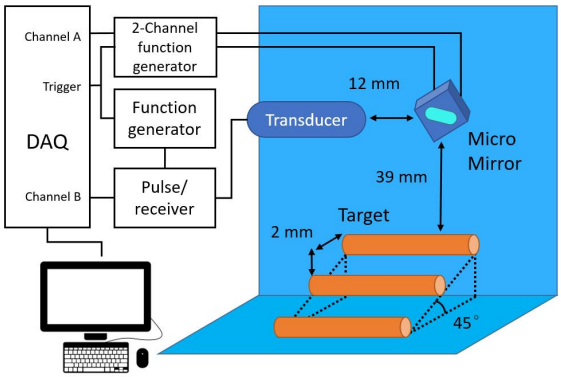


Figure 5.9: Ultrasound imaging test setup.

The pulser/receiver was triggered by a one-channel function generator (33210A, Keysight) with a pulse repetition rate and pulse width of 10 kHz and 1 ns, respectively. The two-axis scanning

mirror was driven by a two-channel function generator (33522B, Keysight). The amplitude and frequency of the two AC driving currents for the fast and slow axes were 50 mA and 500 Hz, and 60 mA and 50 Hz, respectively. The operation of the two function generators were synchronized by the output trgger signal from the data acquisition (DAQ) card (PCI 6251, National Instruments). Bothe the ultrasound echo signals (after pulser/reciever amplification) and the driving current of the fast-axis were digitized by the DAQ card and stored in the computer.

Fig. 5.10a shows the simulated scan path of the focal point of the ultrasound transducer. Since the driving frequency of the fast-axis (500 Hz) is 10 times that of the slow-axis (50 Hz), 5 cycles exist in one raster scanning pattern within a total scanning range of 14 $mm$. With a fast-axis scanning frequency of 500 Hz and a pulse repetition rate of 10 kHz, 20 scan points will be dynamically distributed in one cycle. At each scan point, the ultrasound transducer sends a pulse signal and also detedcts the backscattered echo signal (A-line) from the imaging target. As shown in Fig. 5.10a, with only five cycles in the entire field of view, the average distance between two neighboring scanning cycles is 2.8 $mm$. The ultrasound scan points are therefore sparsely distributed which inevitably results in low (lateral) image resolution. To address this issue, the phase difference of the two driving currents was shifted by $18\circ$ to move the scanning path to the right by 0.14 $mm$ (Fig. 5.10b). By repeating the above phase shift in a series of 20 steps, a total number of 100 cycles can be generated to increse the number of scan points from 100 to 2000. The maximum distance between neighboring scanning points was reduced from 2.8 $mm$ to 0.14 $mm$ accordingly (Fig. 5.10c).

## 5.6 Data Processing and Imaging Reconstruction

The ultrasound data processing and image reconstruction was illustrated in Fig. 5.11. First, as shown in Fig. 5.10c, the phase-shifted scan paths overlap with each other at different locations, which create redundant scan points and cause difficulty in data processing. To address this issue, the scan points on the first half of each scan path was discarded (Fig. 5.11a). The A-line echo signals recorded at the remaining scan points along the same lateral direction were combined to generate a 2D raw B-mode image. The color of the pixels represents the echo signals intensity.

The lateral location of each pixel is determined by the location of the corresponding scan points, while the axial location is determined by its travel time multiplied by sound velocity in water. Next, 2D SAFT (Synthetic Aperture Focusing Technique) [91] was applied on each B-mode image (Fig. 5.11c), followed by a sector transformation based on the real dimensions (Fig. 5.11d). This process was repeated ultil all the B-mode images were formed. It should be noted that the scan points are much denser near the edges of the field-of-view due to lower scan speed. To simplify image reconstruction process, only the center portion (with 800 scan points) of the field-of-view, where the scan points are more evely distributed, is reconstructed. Lastly, all the B-mode images were further stacked together to form a 3D volumetric image (Fig. 5.11e).

Fig. 5.12a and Fig. 5.12b show the typical A-lines echo signals received from the imaging target and the (water) background, respectively. Fig. 5.13a shows one representative raw B-mode image. Since the sound velocity in water (about 1540 m/s) is slower than that in tungsten (about 5184 m/s), the travel distance per pulse (in other words, axial length per pixel in raw data) in water is much shorter than that in tungsten targets, which makes the sound-shaped tungsten wires appear as thin slices. To address this issue, an interpolation algorithm based on the ratio between tungsten and water sound velocity was applied on data inside the target (Fig. 5.13b). The B-mode image after the applying SAFT and sector transformation are shown in Fig. 5.13c and Fig. 5.13d, respectively. The B-mode images were further stacked to form a 3D volumetric image (Fig. 5.14) using $Volview^{®}$. The field of view of the scanning transducer is a cuboid (1 $mm$ in width, 6 $mm$ in height and 6 $mm$ in depth). The lateral resolution is about 1 $mm$, limited by the transducer focal spot size. The lateral and axial intervals between neighboring targets are estimated to be 2.1 $mm$, which is close to the actual distance. The mean diameter of the ultrasound imaged tungsten wires in axial direction was estimated to be 0.5 $mm$, which is also close to the actual diameter.

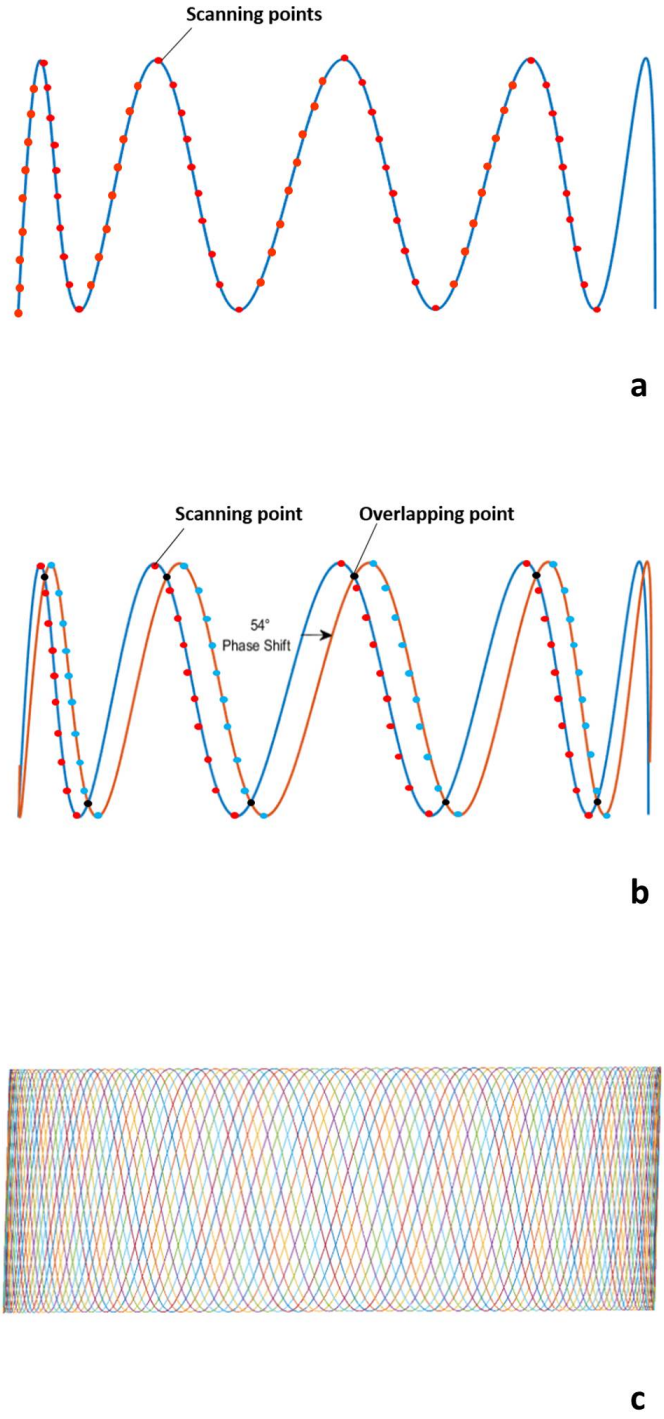


Figure 5.10: (a) Simulated raster scanning pattern; (b) phase shifted scanning pattern; (c) multiple phase-shifted scanning paths combined.

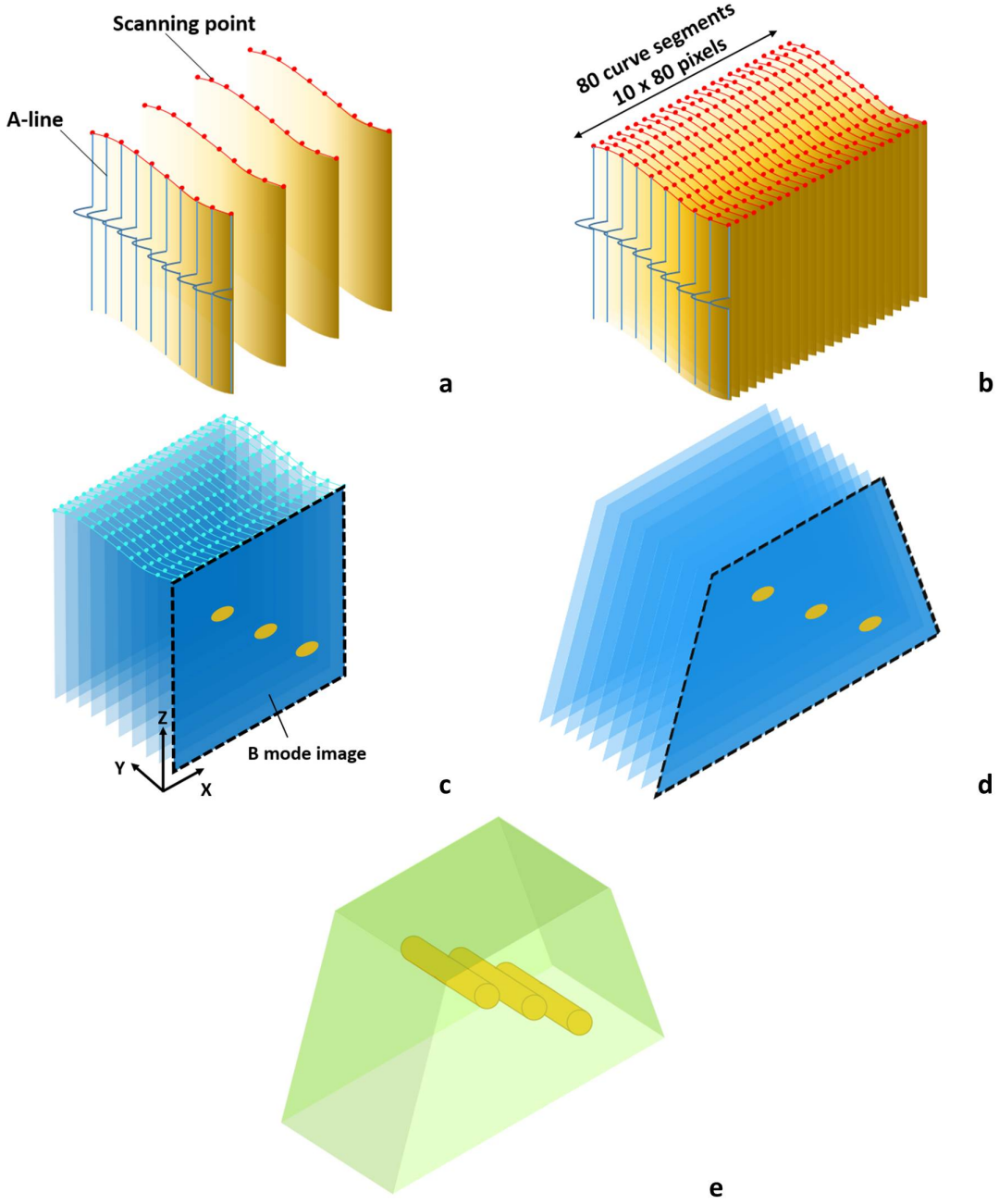


Figure 5.11: Ultrasound image reconstruction process: (a) half of each raster scanning pattern was collected; (b) this process was repeated 20 times; (c) data was sliced on y-direction to form B-mode images; (d) each B-mode slice was transfered to sector; (e) stacking B-mode slices to form a 3D image.

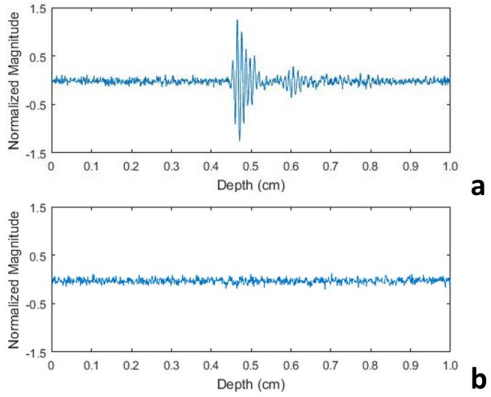


Figure 5.12: A-lines of (a) target and (b) background.

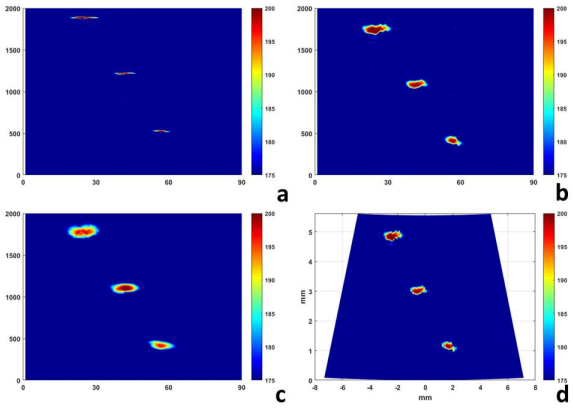


Figure 5.13: (a) A representative B-mode image; (b) B-mode image after interpolation; (c) B-mode image after SAFT; and (d) reshaped to sector images.

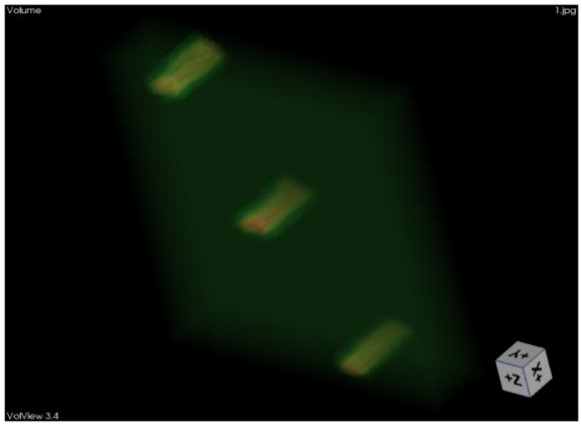


Figure 5.14: 3-D ultrasound image.

# 6. MINIATURIZATION OF TWO-AXIS WATER-IMMERSIBLE SCANNING MIRROR WITH NEW FABRICATION PROCESSES

## 6.1 Introduction

As discussed in previous sections, water-immersible scanning mirrors have been developed to provide fast co-axis scanning of focused optical and ultrasound beams of high-speed ultrasound and photoacoustic microscopy. Different from conventional silicon-based scanning mirrors [92, 93, 94, 95], torsional hinges made of flexible and high-strength thick BoPET (biaxially--oriented polyethylene terephthalate) films were used to avoid possible shock damage in water. However, due to the excellent chemical stability of BoPET, high-resolution patterning of the torsional hinges still poses a challenge. Current fabrication process is based on laser cutting and mechanical dicing followed by multiple steps of manual assembly. It is a slow serial process with low spatial resolution and alignment accuracy, which prevents the miniaturization and batch fabrication of the scanning mirrors.

In this section, a new fabrication process based on double-sided deep reactive ion etching (DRIE) on hybrid silicon-BoPET substrate is reported. It can achieve high spatial resolution and significantly reduce the number of manual assembly steps, making both miniaturization and batch fabrication possible. For demonstration, a two-axis water-immersible scanning mirror was designed, simulated, fabricated and tested. The overall size of the mirror package was reduced down to $5 \times 5 \times 5\ mm^3$ from $10 \times 10 \times 15\ mm^3$ with previous fabrication processed, which is similar to a typical silicon-based micro scanning mirror. This small footprint is suitable for the development of compact ultrasound and photoacoustic imaging systems for handheld and even endoscopic applications.

## 6.2 Design and Simulation

Fig. 6.1 shows the schematic design of the two-axis water-immersible scanning mirror. The main design parameters were listed in Table 6.1. The mirror plate is linked to inner frame by two

fast-axis BoPET hinges. The inner frame and the outer frame are connected by two slow-axis BoPET hinges. The fast-axis hinge are made both wider and shorter than the slow-axis hinges to provide a much higher resonance frequency. Two pairs of permanent magnets with reversed polarization are attached to the backside of the mirror plate. The outer frame is supported with a spacer and mounted onto a inductor coil.

Similar with the electromagnetic actuation principles in previous sections, when an AC driving current (consisting of two frequency components close to the resonance of the two axes) is flowing through the inductor coil, two magnetic torques will be generated to vibrate the mirror plate around the fast-axis hinges and the inner frame (together with the mirror plate) around the slow-axis hinges. However, due to their significantly different resonance frequencies, the vibration of the mirror plate around either fast or slow axis will mainly respond to the current component whose frequency matches its resonance, respectively. Capitalizing upon this intrinsic dynamic filtering effect, the coupling between the two axes is largely suppressed to allow independent control of the two scanning motions even with a single inductor coil.

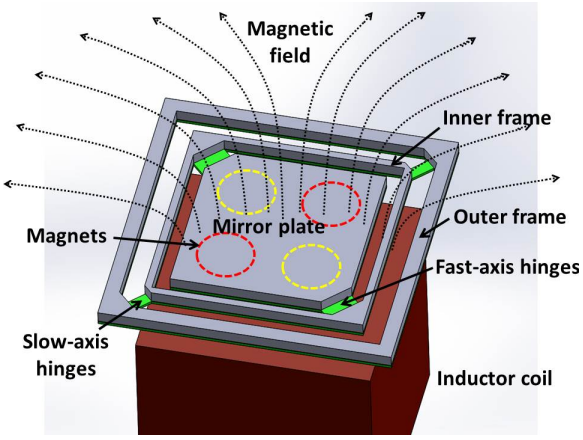


Figure 6.1: Schematic design of the two-axis water-immersible scanning mirror.

A model simulating the relationship among the driving signal, magnetic field intensity and torsional hinge structural deformation was established (Fig. 6.2). The module was consisted of

| | Fast-axis | Slow-axis |
|---|---|---|
| Hinge length ($mm$) | 0.4 | 0.7 |
| Hinge width ($mm$) | 0.56 | 0.2 |
| Hinge thickness ($mm$) | 0.05 | 0.05 |
| Rotational part size ($mm^2$) | $4 \times 4$ | $4.5 \times 4.5$ |
| | BoPET film | |
| Shear modulus ($G$) | 0.02 $GPa$[89] | |
| Density ($\rho_c$) | 1.455 $g/cm^3$[89] | |
| | Inductor coil | |
| Inductance | 1 $mH$ | |
| Coil length | 2 $mm$ | |
| Coil diameter | 3 $mm$ | |
| | Permanent magnet | |
| Diameter | 1.5 $mm$ | |
| Height | 0.7 $mm$ | |
| Density | 7.5 $g/cm^3$ | |
| | Viscosity[90] | |
| Water | 1.002 $mPa-s$ | |
| Air | 18.6 $\mu Pa-s$ | |

Table 6.1: Main design parameters of two-axis micro scanning mirror.

two modules: structural module and electromagnetic module. Structural module was composed of BoPET hinges, silicon mirror plate and frame. The resonant frequencies could be acquired by the first eigenmodes of this module. The electromagnetic module was composed of permanent magnets and inductor coil. Since the number of turns of the inductor coil and the remanent flux density of the permanent magnet were not provided by the manufacture, two characterization signals were first used to determine these two parameters (Fig. 6.3). Given driving signal frequency and amplitude, the electromagnetic field around the inductor coil could be calculated. Combined with the property of the permanent magnet, the torque applied upon the permanent magnets could be simulated. Iterating between these two modules, the scanning angles of the mirror plate in response to different driving signals could be calculated. Fig. 6.4 shows the simulated first eigenmodes of fast-axis and slow-axis. In air, the resonant frequencies were simulated to be 405 Hz (fast-axis) and 181 Hz (slow-axis). When immersed in water, the resonant frequencies were reduced to 345 Hz (fast-axis) and 153 Hz (slow-axis).

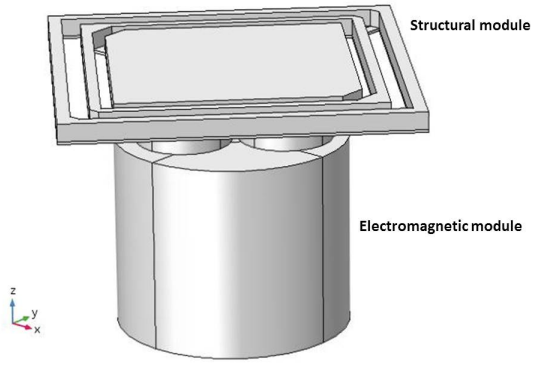


Figure 6.2: Simulation structure layout.

When driven at resonant frequencies, the relationship between the driving signal amplitudes and scanning angles was also simulated in this module (Fig. 6.5). Since the shear modulus of BoPET is small, it is possible to drive slow-axis using DC current without significantly increasing the power consumption (Fig. 6.5). Both the AC and DC driving plots shows a linear relationship between the scanning angles and driving current amplitudes.

## 6.3 Fabrication and Assembly

The fabrication process was conducted as follows. First, a 200 $\mu$m silicon wafer was bonded to a 50 $\mu$m thick BoPET film (Fig. 6.7a). After evaporating a Cr/Cu seed layer on the backside of BoPET film, a 5 $\mu$m thick Ni mask was electroplated to serve as a mask for BoPET etching (Fig. 6.7b). The BoPET film was etched with a cryogenic process (Fig. 6.7c). After removing the Ni mask, an 0.4 $\mu$m thick aluminmum layer was deposited on the silicon wafer as a mask for cryogenic silicon etching to form the mirror plate, inner frame and outer frame (Fig. 6.7d). Table 6.2 lists the process parameters of the BoPET and silicon etching. Next, permanent magnets were assembled to the mirror plate by using a thin acrylic template (Fig. 6.7e). After the permanent magnets were securely bonded, the acrylic template was reomved. Lastly, an acrylic spacer was bonded to the outer frame (Fig. 6.7f). After attaching the spacer to the inductor coil, this scanning mirror was ready for testing. Fig. 6.8 shows a fully assembled scanning mrror with a zoom-in view

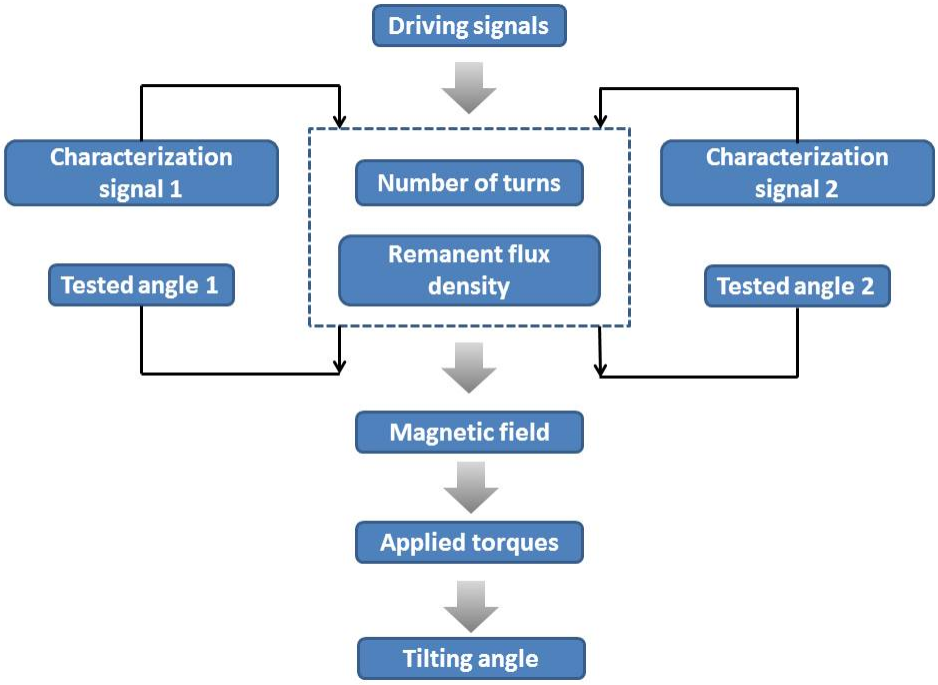


Figure 6.3: Simulation process.

of one etched BoPET hinge for the slow axis.

## 6.4 Characterization

A laser tracing method was used to characterize the scanning performance of the prototype in both air and water. A CW laser was projected on the center of the mirror plate at an incident angle of $45^{\circ}$ and reflected vertically onto a ruler placed at 70 mm away from the mirror plate. The scanning angle was calculated based on the length of the laser trace on the ruler.

First, the resonant frequencies were characterized. The resonant frequency is defined as the following: at fixed driving current amplitude, at which frequency the scanning range reaches its maximum. In air, the resonant frequencies of the fast- and slow-axis were determined to be 420 Hz and 190 Hz (Fig. 6.9a) in air and water, respectively. When immersed in water, the resonant frequency were reduced to 330 Hz and 160 Hz (Fig. 6.9b), respectively.

In addition, the optical tilting angles of the fast and slow axes (at their resonant frequencies) driven by AC currents with different amplitudes were characterized (Fig. 6.10). The scanning

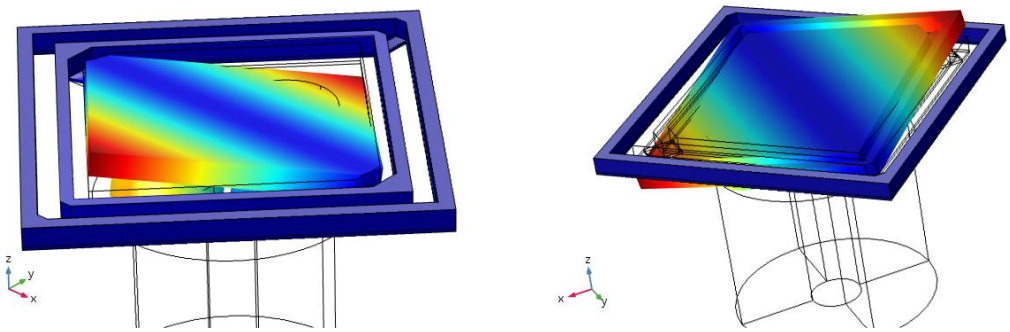

Figure 6.4: Simulated first eigenmodes of: fast-axis (left) and slow-axis (rignt).

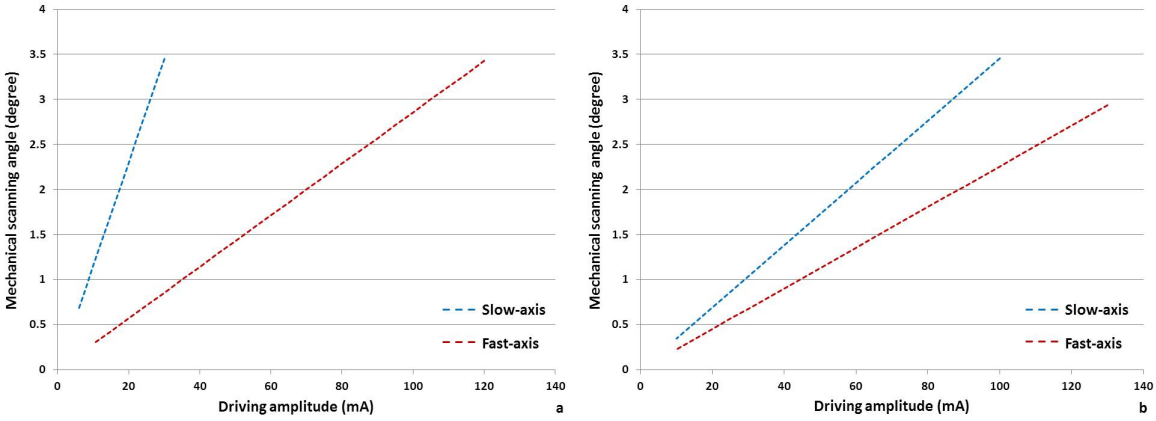


Figure 6.5: Simulated mechanical scanning angles at different driving current amplitudes at resonant frequencies in (a) air and (b) water.

angle increases almost linearly with respect to the current amplitudes. An mechanical angle of $3^{\circ}$ was achieved in air (with 32 mA for slow-axis and 101 mA for fast-axis). For this mirror, it is also possible to drive the slow-axis at DC, achieving a similar field of view without significantly increasing driving power (Fig. 6.11).

Raster scanning pattern with both axes actuated was also characterized. Both driving signals were synchronized and the phases locked. Fast- axis were driven at its resonant frequency (330 Hz, 130 mA in water). Slow-axis driving frequencies were set at 110 Hz, 260 mA (Fig. 6.12a), 82.5 Hz, 350 mA (Fig. 6.12b), 66 Hz, 410 mA (Fig. 6.12c) and 55 Hz, 430 mA (Fig. 6.12d).

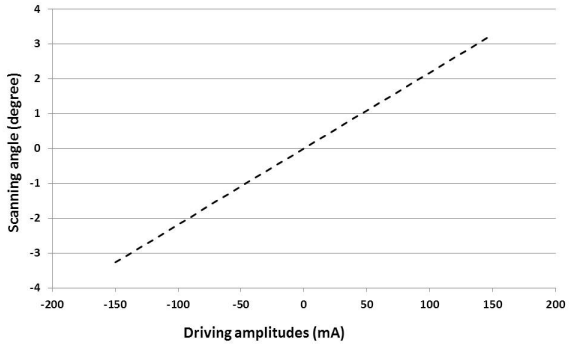


Figure 6.6: Simulated mechanical scanning angles at different driving current amplitudes at DC driving.

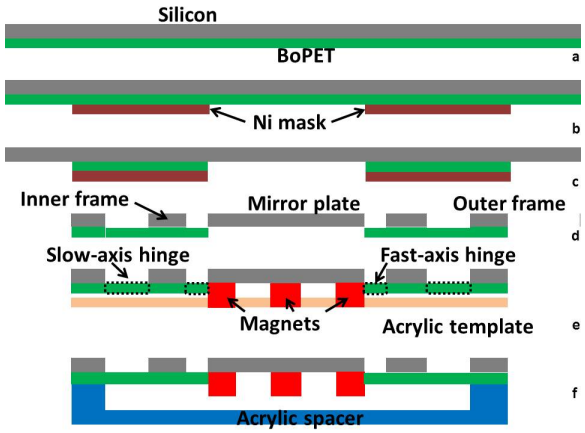


Figure 6.7: Fabrication and assembly process.

The driving current amplitudes were tuned to keep a $\pm 3^{\circ}$ mechanical scanning angle for both axes. There is a slight vertical shift in the fast scanning cycles. The main reason for this tilting is because when the slow-axis is actuated, the orientation of the two magnets around the fast-axis had already been tilted to a certain amount of degrees. However, as shown in Fig. 6.12, the raster scanning patterns were stable and repeatable. Therefore, once the scanning pattern is calibrated, this shift should not be a big concern for retriving the locations of the scan points in image reconstruction.

| | BoPET | silicon |
|---|---|---|
| Temperature | $-80°C$ | $-110°C$ |
| Pressure | 30 mtorr | 30 mtorr |
| Ar | 80 sccm | 0 |
| $O_2$ | 30 sccm | 30 sccm |
| $SF_6$ | 0 | 90 sccm |
| RF power | 150 W | 10 W |
| ICP power | 300 W | 600 W |
| Etch rate | $0.21\mu m/min$ | $1\mu m/min$ |
| Aspect ratio | 7.14 | 55 |

Table 6.2: Process parameters for BoPET and silicon etching.

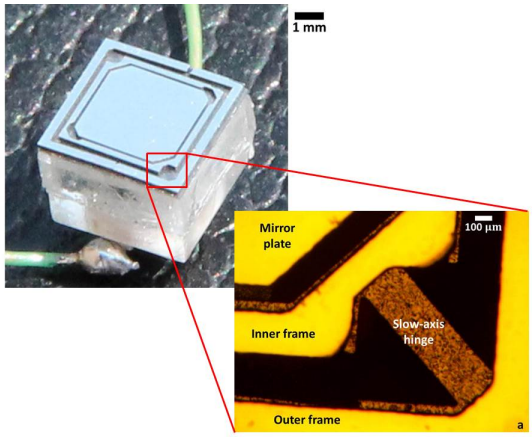


Figure 6.8: Left: fully assembled prototype; right: zoom-in etch result.

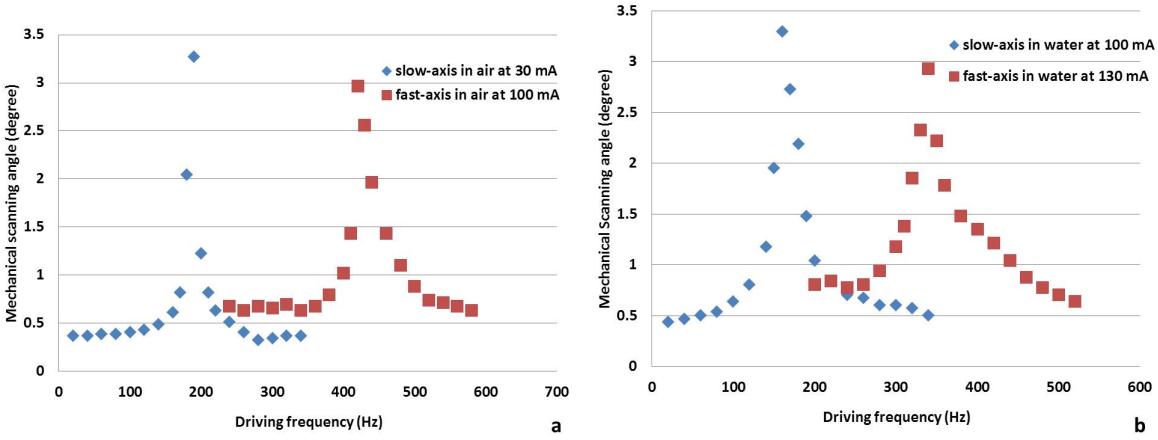


Figure 6.9: Resonant frequencies in (a) air and (b) water.

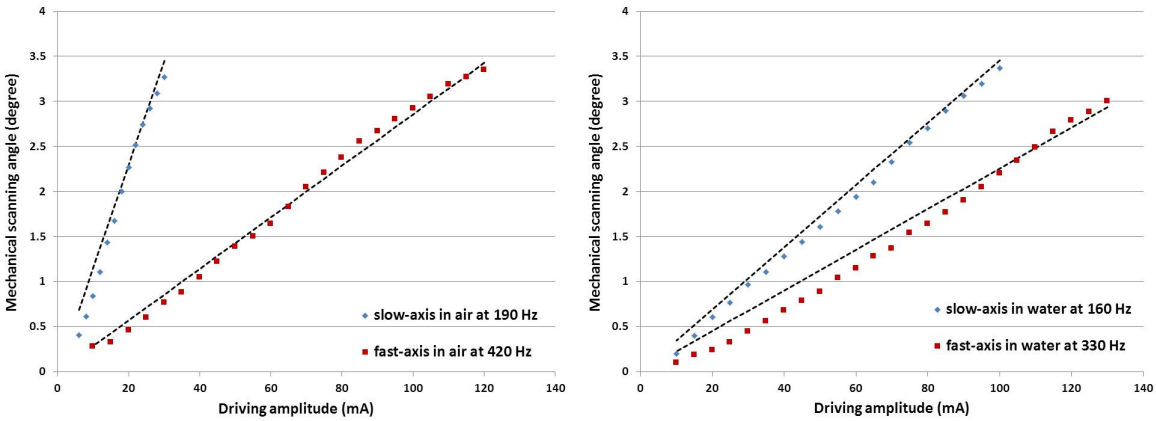


Figure 6.10: Scanning angles at resonant frequencies (a) in air and (b) in water; dashed lines are simulated results.

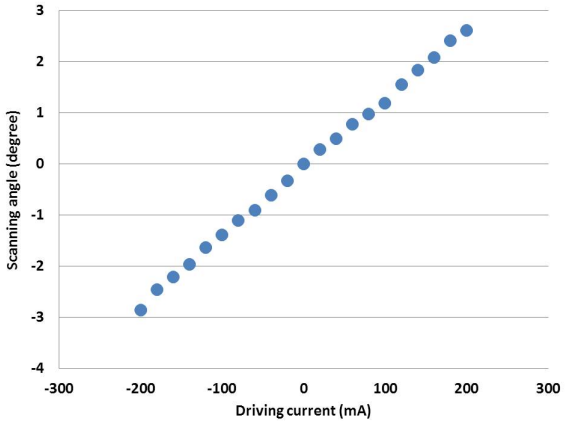


Figure 6.11: DC driving test result.

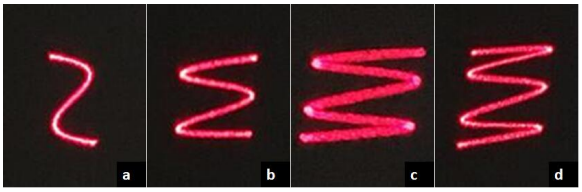


Figure 6.12: Raster scanning results.

# 7. A LARGE FIELD OF VIEW IMPACT RESISTANT TWO-AXIS SCANNING MIRROR

## 7.1 Introduction

Autonomous driving has emerged as an attractive topic since recent years. LiDAR (light detection and ranging) systems have been used in autonomous vehicles for obstacle detection and avoidance to navigate safely through environments. In order to be feasibly installed in commercial vehicles, one primary requirement of these LiDAR systems is that they have to be capable of wide angle scanning at a at least 30 Hz scanning frequency. One popular solution is to use phased array [96]. By controlling the excitation time delay of different laser fibers, the laser beam focal point and focal length can be alternated. After collecting the reflected or backscattered laser signals, object detection or ranging becomes possible.

There are several drawbacks in phased array if integrated in commercial vehicles. First, the received signal amplitude is limited by the fiber numerical aperture, which is usually small. Admittedly, the fired detection laser power can be large, after reflection or scattering, the signal to be collected is low. Moreover, given the small diameter of the fibers, the numerical aperture of these fibers is limited, which further reduces the received laser signal amplitude. Consequently, the SNR (signal to noise ratio) of the reconstructed image could be an concern. Second, since the phased array system is controlled digitally, the system is inevitably complex and expensive.

In this chapter, a new low cost large field of view scanning mirror fabricated from BoPET films is proposed. As mentioned in previous chapters, the BoPET treatment methods, including laser micromachining and reactive ion etching, can be fast and cheap. Combining with its low shear modulus property, it is possible to achieve large scanning angle at the same time maintaining its impact resistance nature. In previous chapters, torsional mode of the BoPET film has been explored. It is possible to achieve $\pm 10^{\circ}$ scanning field of view without significant degradation. To enlarge the field of view, bending mode is explored in the new scanning mirror, extending the field of view to $\pm 60^{\circ}$.

## 7.2 Design and Assembly

Fig. 7.1a shows the schematic hinge design of the large angle scanning mirror. Fig. 7.1b shows the overall design of the scanning mirror module. The main design parameters were listed in Table 7.1. The mirror plate and a pair of permanent magnets are bonded inside the inner frame. Connected by a pair of torsional hinges (fast-axis), the inner frame is connected to the outer frame. A bending hinge (slow-axis) is used to link the outer frame to anchor. Four inductor coils are arranged on both sides of the anchor to provide actuation electromagnetic field. To drive the fast-axis, top two inductor coils are actuated by the same driving signal whereas the bottom two inductors driven by a 180 degree different driving signal: the two permanent magnets rotate the mirror plate around the fast-axis hinges. To drive the slow-axis, all four inductor coils are driven by one signal, providing an uniform electromagnetic field over the permanent magnets. Therefore, a two-axis driving can be achieved.

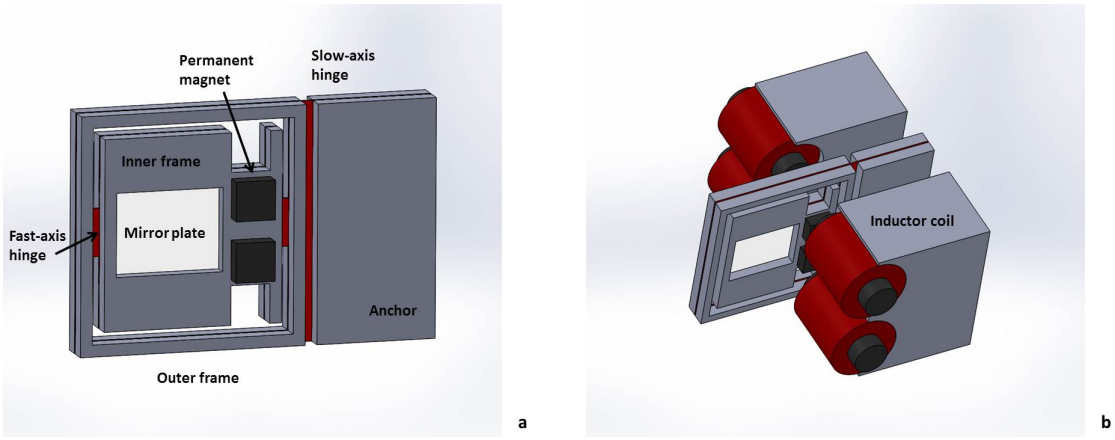


Figure 7.1: Schematic design of (a) the bending hinge and torsional hinge layout and (b) module layout including actuators.

The fabrication and assembly process was conducted as follows. First, a 150 $\mu$m thick BoPET film sheet, acrylic inner frames and outer frames are micromachined. The inner frame is first bonded to the BoPET film sheet. Then the permanent magnets attached to the BoPET film. Before

| | Fast-axis | Slow-axis |
|---|---|---|
| Hinge length ($mm$) | 0.7 | 1 |
| Hinge width ($mm$) | 0.4 | 20 |
| Hinge thickness ($mm$) | 0.15 | 0.15 |
| Rotational part size ($mm^2$) | $16 \times 18$ | $18 \times 20$ |
| | BoPET film | |
| Shear modulus ($G$) | 0.02 $GPa$[89] | |
| Density ($\rho_c$) | 1.455 $g/cm^3$[89] | |
| | Inductor coil | |
| Inductance | 33 $mH$ | |
| Coil length | 15 $mm$ | |
| Coil diameter | 8 $mm$ | |
| | Permanent magnet | |
| Length | 2 $mm$ | |
| Height | 1.3 $mm$ | |
| Density | 7.5 $g/cm^3$ | |

Table 7.1: Main design parameters of the large angle two-axis scanning mirror.

bonding the outer frame and anchors, the mirror plate is attached to the center of BoPET film. Lastly, inductor coils are fixed to the anchor. After curing the bonding agency, the prototype is ready to be tested. Fig. 7.2 shows an assembled prototype.

### 7.3 Characterization

A laser tracing method was used to characterize the scanning performance of the prototype in both air and water. A CW laser was projected on the center of the mirror plate at an incident angle of $45^\circ$ and reflected vertically onto a ruler placed at 70 mm away from the mirror plate. The scanning angle was calculated based on the length of the laser trace on the ruler.

The resonant frequencies were characterized. The resonant frequency is defined as the following: at fixed driving current amplitude, at which frequency the scanning range reaches its maximum. In air, the resonant frequencies of the fast- and slow-axis were determined to be 260 Hz and 30 Hz (Fig. 7.3).

Raster scanning pattern with both axes actuated was also characterized. Both driving signals were synchronized and the phases locked. Fast- axis and slow-axis were both driven at their res-

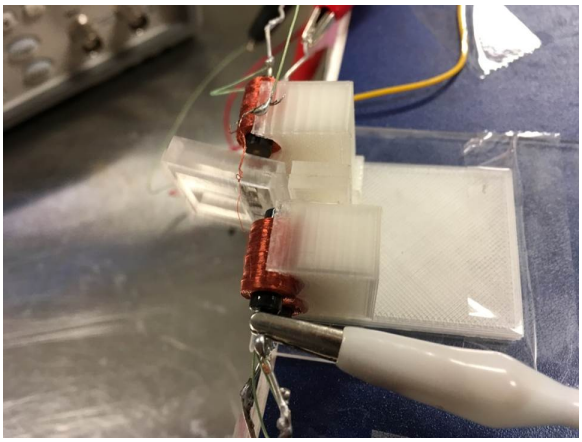

Figure 7.2: An assembled prototype.

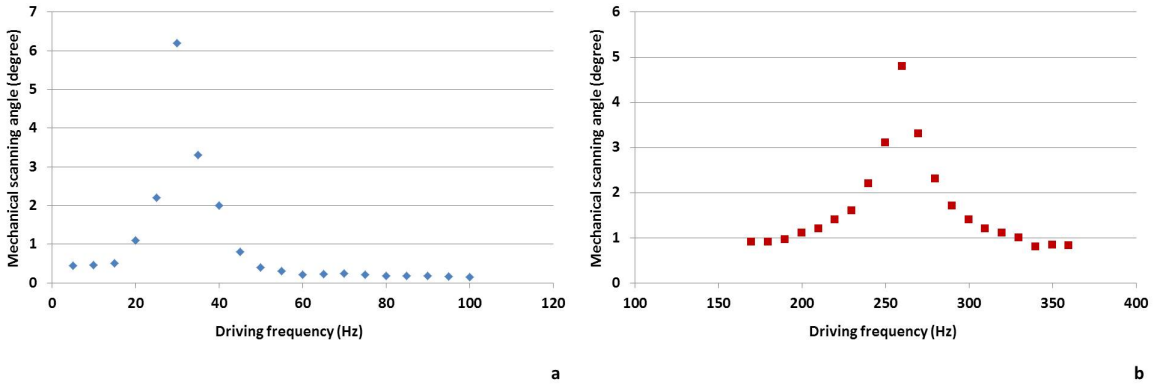


Figure 7.3: Resonance frequency test of (a) slow-axis and (b) fast-axis.

onant frequency (Fig. 7.4). Fast-axis was driven at 150 mA and slow-axis at 100 mA. Fast-axis achieved a $\pm 10^{\circ}$ field of view whereas slow-axis $\pm 60^{\circ}$. There is a slight vertical shift in the fast scanning cycles. The main reason for this tilting is because when the slow-axis is actuated, the orientation of the two magnets around the fast-axis had already been tilted to a certain amount of degrees. However, as shown in Fig. 7.4, the raster scanning patterns were stable and repeatable. Therefore, once the scanning pattern is calibrated, this shift should not be a big concern for retriving the locations of the scan points in image reconstruction.

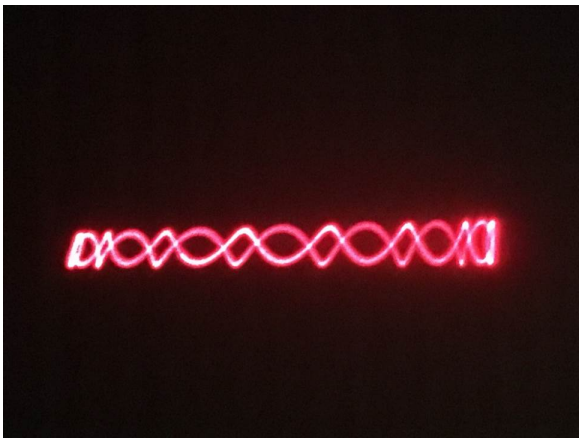

Figure 7.4: Raster scanning result.

# 8. CONCLUSION AND FUTURE WORK

## 8.1 Conclusion

A new polymer material, BoPET (biaxially-oriented polyethylene terephthalate) has been studied and fabricated to serve torsional hinges of water-immersible scanning mirrors for ultrasound and photoacoustic microscopy purposes. Both single-axis and two-axis prototypes were designed, fabricated and characterized. Different from conventional MEMS scanning mirrors with silicon torsional hinges, this new material ensures new scanning mirrors resistive to shocking in liquid because of its lower shear modulus. Without increasing the complexity of fabrication, this new design can achieve repeatable and stable raster scanning patterns in liquid, which is required by ultrasound propagation. Ultrasound images have been successfully demonstrated using these prototypes.

New electromagnetic actuators based on dynamic filtering effect have been developed to miniaturize the package size of the two-axis water-immersible scanning mirror. These new electromagnetic actuators have several unique advantages over traditional actuators: (1) It only requires one inductor coil to drive both axes, making it possible to further reduce the size of the scanning mirror package. (2) The coupling effect between two scanning axes is minimized mechanically, providing a more stable, predictable and repeatable raster scanning pattern. (3) Independent control upon each axis becomes possible. The process characterization and mechanical modeling have been performed and a prototype fabricated. To improve the lateral resolution, a phase shifting method has been proposed. Both B-mode and 3D ultrasound images have been reconstructed using the prototype.

Novel BoPET treatment recipes have been developed to achieve high resolution. Different from previous prototypes which are fabricated by laser micromachining, a new miniaturized two-axis water-immersible scanning mirror is processed by cryogenic reactive ion etching instrument. A significantly higher resolution can be achieved, therefore making the package size comparable to conventional silicon based MEMS scanning mirrors. Furthermore, manual assembly has

been minimized in this prototype, making batch fabrication possible. Table 8.1 summarizes the performances of different prototypes and their package sizes.

| | Two-axis multiple actuator | Single-axis single actuator | Two-axis single actuator | Miniaturized two-axis single actuator |
|---|---|---|---|---|
| Fast-axis in air (Hz) | 320 | 250 | 720 | 420 |
| Fast-axis in water (Hz) | 230 | 210 | 72 | 190 |
| Slow-axis in air (Hz) | 24 | NA | 690 | 330 |
| Slow-axis in water (Hz) | 13 | NA | 55 | 160 |
| Tested field of view (degree) | $\pm 15$ | $\pm 12$ | $\pm 10$ | $\pm 3$ |
| Package size ($mm^3$) | 16×16×13 | 7×5×7 | 10×10×15 | 5×5×5 |

Table 8.1: Performances and package sizes of different prototypes.

## 8.2 Future Work

For the miniaturized water-immersible scanning mirror, permanent magnet fabrication process needs to be further studied. In current prototype, permanent magnets are first attached to an acrylic template. This template is later aligned to the mirror plate with permanent magnets bonded. After epoxy between permanent magnets and mirror plate cures, the template is removed. Currently, this process involves manual assembly and the alignment accuracy is not guaranteed. To improve the scanning performance and output reliability, a novel permanent magnet fabrication process that deposits directly onto the mirror plate is preferred to further reduce the cost of mass production.

# REFERENCES


[1] L. J. Hornbeck, "Digital light processing for high-brightness high-resolution applications," in *Projection Displays III*, vol. 3013, pp. 27–41, International Society for Optics and Photonics, 1997.

[2] D. Hah, P. R. Patterson, H. D. Nguyen, H. Toshiyoshi, and M. C. Wu, "Theory and experiments of angular vertical comb-drive actuators for scanning micromirrors," *IEEE Journal of Selected Topics in Quantum Electronics*, vol. 10, no. 3, pp. 505–513, 2004.

[3] L. Fan and M. C. Wu, "Two-dimensional optical scanner with large angular rotation realized by self-assembled micro-elevator," in *Broadband Optical Networks and Technologies: An Emerging Reality/Optical MEMS/Smart Pixels/Organic Optics and Optoelectronics. 1998 IEEE/LEOS Summer Topical Meetings*, pp. II–107, IEEE, 1998.

[4] V. A. Aksyuk, F. Pardo, C. A. Bolle, S. Arney, C. R. Giles, and D. J. Bishop, "Lucent microstar micromirror array technology for large optical crossconnects," in *MOEMS and Miniaturized Systems*, vol. 4178, pp. 320–325, International Society for Optics and Photonics, 2000.

[5] J.-H. Lee, Y.-C. Ko, D.-H. Kong, J.-M. Kim, K. B. Lee, and D.-Y. Jeon, "Design and fabrication of scanning mirror for laser display," *Sensors and Actuators A: Physical*, vol. 96, no. 2-3, pp. 223–230, 2002.

[6] P. R. Patterson, D. Hah, H. Chang, H. Toshiyoshi, and M. C. Wu, "An angular vertical comb drive for scanning micromirrors," in *IEEE/LEOS International Conference on Optical MEMS*, p. 25, 2001.

[7] J. Sun, S. J. Lee, L. Wu, M. Sarntinoranont, and H. Xie, "Refractive index measurement of acute rat brain tissue slices using optical coherence tomography," *Optics Express*, vol. 20, no. 2, pp. 1084–1095, 2012.

[8] S. Pal and H. Xie, "Fabrication of robust electrothermal mems devices using aluminum–tungsten bimorphs and polyimide thermal isolation," *Journal of Micromechanics and Microengineering*, vol. 22, no. 11, p. 115036, 2012.

[9] Y. Xu, J. Singh, T. Selvaratnam, and N. Chen, "Two-axis gimbal-less electrothermal micromirror for large-angle circumferential scanning," *IEEE Journal of Selected Topics in Quantum Electronics*, vol. 15, no. 5, pp. 1432–1438, 2009.

[10] K. Jia, S. R. Samuelson, and H. Xie, "High-fill-factor micromirror array with hidden bimorph actuators and tip–tilt-piston capability," *Journal of Microelectromechanical Systems*, vol. 20, no. 3, pp. 573–582, 2011.

[11] T. Naono, T. Fujii, M. Esashi, and S. Tanaka, "Non-resonant 2-d piezoelectric mems optical scanner actuated by nb doped pzt thin film," *Sensors and Actuators A: Physical*, vol. 233, pp. 147–157, 2015.

[12] K. H. Koh, T. Kobayashi, and C. Lee, "Investigation of piezoelectric driven mems mirrors based on single and double s-shaped pzt actuator for 2-d scanning applications," *Sensors and Actuators A: Physical*, vol. 184, pp. 149–159, 2012.

[13] U. Baran, D. Brown, S. Holmstrom, D. Balma, W. O. Davis, P. Muralt, and H. Urey, "Resonant pzt mems scanner for high-resolution displays," *Journal of Microelectromechanical Systems*, vol. 21, no. 6, pp. 1303–1310, 2012.

[14] C. Liu, T. Tsao, G.-B. Lee, J. T. Leu, W. Y. Yong, Y.-C. Tai, and C.-M. Ho, "Out-of-plane magnetic actuators with electroplated permalloy for fluid dynamics control," *Sensors and Actuators A: Physical*, vol. 78, no. 2-3, pp. 190–197, 1999.

[15] X. Lv, W. Wei, X. Mao, Y. Chen, J. Yang, and F. Yang, "A novel mems electromagnetic actuator with large displacement," *Sensors and Actuators A: Physical*, vol. 221, pp. 22–28, 2015.

[16] J. W. Judy and R. S. Muller, "Magnetically actuated, addressable microstructures," *Journal of Microelectromechanical Systems*, vol. 6, no. 3, pp. 249–256, 1997.

[17] T. Bourouina, E. Lebrasseur, G. Reyne, A. Debray, H. Fujita, A. Ludwig, E. Quandt, H. Muro, T. Oki, and A. Asaoka, "Integration of two degree-of-freedom magnetostrictive actuation and piezoresistive detection: application to a two-dimensional optical scanner," *Journal of Microelectromechanical Systems*, vol. 11, no. 4, pp. 355–361, 2002.

[18] D. W. Wine, M. P. Helsel, L. Jenkins, H. Urey, and T. D. Osborn, "Performance of a biaxial mems-based scanner for microdisplay applications," in *MOEMS and Miniaturized Systems*, vol. 4178, pp. 186–197, International Society for Optics and Photonics, 2000.

[19] M. F. Aimi, M. P. Rao, N. C. MacDonald, A. S. Zuruzi, and D. P. Bothman, "High-aspect-ratio bulk micromachining of titanium," *Nature Materials*, vol. 3, no. 2, p. 103, 2004.

[20] M. Mehregany, C. A. Zorman, S. Roy, A. J. Fleischman, W. C.-H., and N. Rajan, "Silicon carbide for microelectromechanical systems," *International Materials Reviews*, vol. 45, no. 3, pp. 85–108, 2000.

[21] S. Desai, A. Netravali, and M. Thompson, "Carbon fibers as a novel material for high-performance microelectromechanical systems (mems)," *Journal of Micromechanics and Microengineering*, vol. 16, no. 7, p. 1403, 2006.

[22] S. T. Holmstrom, U. Baran, and H. Urey, "Mems laser scanners: a review," *Journal of Microelectromechanical Systems*, vol. 23, no. 2, pp. 259–275, 2014.

[23] K. E. Petersen, "Silicon torsional scanning mirror," *IBM Journal of Research and Development*, vol. 24, no. 5, pp. 631–637, 1980.

[24] D. Dickensheets and G. Kino, "Micromachined scanning confocal optical microscope," *Optics Letters*, vol. 21, no. 10, pp. 764–766, 1996.

[25] W. Piyawattanametha, H. Ra, M. J. Mandella, K. Loewke, T. D. Wang, G. S. Kino, O. Solgaard, and C. H. Contag, "3-d near-infrared fluorescence imaging using an mems-based miniature dual-axis confocal microscope," *IEEE Journal of Selected Topics in Quantum Electronics*, vol. 15, no. 5, pp. 1344–1350, 2009.

[26] Y. Pan, H. Xie, and G. K. Fedder, "Endoscopic optical coherence tomography based on a microelectromechanical mirror," *Optics Letters*, vol. 26, no. 24, pp. 1966–1968, 2001.

[27] K. Isamoto, K. Totsuka, T. Suzuki, T. Sakai, A. Morosawa, C. Chong, H. Fujita, and H. Toshiyoshi, "A high speed mems scanner for 140-khz ss-oct," in *Optical MEMS and Nanophotonics (OMN), 2011 International Conference on*, pp. 73–74, IEEE, 2011.

[28] H. Urey, D. W. Wine, and J. R. Lewis, "Scanner design and resolution trade-offs for miniature scanning displays," in *Flat Panel Display Technology and Display Metrology*, vol. 3636, pp. 60–69, International Society for Optics and Photonics, 1999.

[29] U. Hofmann, F. Senger, F. Soerensen, V. Stenchly, B. Jensen, and J. Janes, "Biaxial resonant 7mm-mems mirror for automotive lidar application," in *Optical MEMS and Nanophotonics (OMN), 2012 International Conference on*, pp. 150–151, IEEE, 2012.

[30] Ç. Ataman, S. Lani, W. Noell, and N. De Rooij, "A dual-axis pointing mirror with moving-magnet actuation," *Journal of Micromechanics and Microengineering*, vol. 23, no. 2, p. 025002, 2012.

[31] R. Lemons and C. Quate, "Acoustic microscope-scanning version," *Applied Physics Letters*, vol. 24, no. 4, pp. 163–165, 1974.

[32] I. Cespedes, J. Ophir, H. Ponnekanti, and N. Maklad, "Elastography: elasticity imaging using ultrasound with application to muscle and breast in vivo," *Ultrasonic Imaging*, vol. 15, no. 2, pp. 73–88, 1993.

[33] S. Chen, M. W. Urban, C. Pislaru, R. Kinnick, Y. Zheng, A. Yao, and J. F. Greenleaf, "Shear-wave dispersion ultrasound vibrometry (sduv) for measuring tissue elasticity and viscosity," *IEEE Transactions on Ultrasonics, Ferroelectrics, and Frequency Control*, vol. 56, no. 1, pp. 55–62, 2009.

[34] J. Bereiter-Hahn, L. Karl, H. Lüers, and M. Vöth, "Mechanical basis of cell shape: investigations with the scanning acoustic microscope," *Biochemistry and Cell Biology*, vol. 73, no. 7-8, pp. 337–348, 1995.

[35] H. Lüers, K. Hillmann, J. Litniewski, and J. Bereiter-Hahn, "Acoustic microscopy of cultured cells," *Cell Biophysics*, vol. 18, no. 3, p. 279, 1991.

[36] J. Hildebrand, D. Rugar, R. Johnston, and C. Quate, "Acoustic microscopy of living cells," *Proceedings of the National Academy of Sciences*, vol. 78, no. 3, pp. 1656–1660, 1981.

[37] R. Johnston, A. Atalar, J. Heiserman, V. Jipson, and C. Quate, "Acoustic microscopy: resolution of subcellular detail," *Proceedings of the National Academy of Sciences*, vol. 76, no. 7, pp. 3325–3329, 1979.

[38] H. F. Zhang, K. Maslov, G. Stoica, and L. V. Wang, "Functional photoacoustic microscopy for high-resolution and noninvasive in vivo imaging," *Nature Biotechnology*, vol. 24, no. 7, p. 848, 2006.

[39] K. Maslov, H. F. Zhang, S. Hu, and L. V. Wang, "Optical-resolution photoacoustic microscopy for in vivo imaging of single capillaries," *Optics Letters*, vol. 33, no. 9, pp. 929–931, 2008.

[40] Y. Zhou, J. Yao, and L. V. Wang, "Tutorial on photoacoustic tomography," *Journal of Biomedical Optics*, vol. 21, no. 6, p. 061007, 2016.

[41] J. Yao and L. Wang, "Biomedical optics & medical imaging eavesdropping on oxygen metabolism,"

[42] L. V. Wang and S. Hu, "Photoacoustic tomography: in vivo imaging from organelles to organs," *Science*, vol. 335, no. 6075, pp. 1458–1462, 2012.

[43] C. Yeh, B. T. Soetikno, S. Hu, K. I. Maslov, and L. V. Wang, "Microvascular quantification based on contour-scanning photoacoustic microscopy," *Journal of Biomedical Optics*, vol. 19, no. 9, p. 096011, 2014.

[44] W. C. Mabie, T. G. DiSessa, L. G. Crocker, B. M. Sibai, and K. L. Arheart, "A longitudinal study of cardiac output in normal human pregnancy," *American Journal of Obstetrics and Gynecology*, vol. 170, no. 3, pp. 849–856, 1994.

[45] B. W. Drinkwater and P. D. Wilcox, "Ultrasonic arrays for non-destructive evaluation: A review," *NDT & e International*, vol. 39, no. 7, pp. 525–541, 2006.

[46] C. Liu, *Foundations of MEMS*. Pearson Education India, 2012.

[47] D. S. Greywall, P. A. Busch, F. Pardo, D. W. Carr, G. Bogart, and H. T. Soh, "Crystalline silicon tilting mirrors for optical cross-connect switches," *Journal of Microelectromechanical Systems*, vol. 12, no. 5, pp. 708–712, 2003.

[48] K. B. Lee and Y.-H. Cho, "Laterally driven electrostatic repulsive-force microactuators using asymmetric field distribution," *Journal of Microelectromechanical Systems*, vol. 10, no. 1, pp. 128–136, 2001.

[49] G. N. Nielson and G. Barbastathis, "Dynamic pull-in of parallel-plate and torsional electrostatic mems actuators," *Journal of Microelectromechanical Systems*, vol. 15, no. 4, pp. 811–821, 2006.

[50] V. A. Aksyuk, M. E. Simon, F. Pardo, S. Arney, D. Lopez, and A. Villanueva, "Optical mems design for telecommunications applications," in *Solid-state Sensor, Actuator and Microsystems Workshop, Hilton Head Island, South Carolina*, pp. 1–6, 2002.

[51] W. C. Tang, T.-C. H. Nguyen, M. W. Judy, and R. T. Howe, "Electrostatic-comb drive of lateral polysilicon resonators," *Sensors and Actuators A: Physical*, vol. 21, no. 1-3, pp. 328–331, 1990.

[52] A. Selvakumar and K. Najafi, "Vertical comb array microactuators," *Journal of Microelectromechanical Systems*, vol. 12, no. 4, pp. 440–449, 2003.

[53] Y. Nemirovsky and O. Bochobza-Degani, "A methodology and model for the pull-in parameters of electrostatic actuators," *Journal of Microelectromechanical Systems*, vol. 10, no. 4, pp. 601–615, 2001.

[54] L. A. Rocha, E. Cretu, and R. F. Wolffenbuttel, "Analysis and analytical modeling of static pull-in with application to mems-based voltage reference and process monitoring," *Journal of Microelectromechanical Systems*, vol. 13, no. 2, pp. 342–354, 2004.

[55] O. Degani, E. Socher, A. Lipson, T. Lejtner, D. J. Setter, S. Kaldor, and Y. Nemirovsky, "Pull-in study of an electrostatic torsion microactuator," *Journal of Microelectromechanical Systems*, vol. 7, no. 4, pp. 373–379, 1998.

[56] U. Krishnamoorthy, "Self-aligned vertical combdrive actuators for optical scanning micromirrors," in *Proc. 2001 IEEE/LEOS Int. Conf. on Optical MEMS (Optical MEMS 2001)*, pp. 41–42, 2001.

[57] U. Krishnamoorthy, D. Lee, and O. Solgaard, "Self-aligned vertical electrostatic combdrives for micromirror actuation," *Journal of Microelectromechanical Systems*, vol. 12, no. 4, pp. 458–464, 2003.

[58] S. Prasanna and S. M. Spearing, "Materials selection and design of microelectrothermal bimaterial actuators," *Journal of Microelectromechanical Systems*, vol. 16, no. 2, pp. 248–259, 2007.

[59] K. Luo, Z. Shi, J. Varesi, and A. Majumdar, "Sensor nanofabrication, performance, and conduction mechanisms in scanning thermal microscopy," *Journal of Vacuum Science & Technology B: Microelectronics and Nanometer Structures Processing, Measurement, and Phenomena*, vol. 15, no. 2, pp. 349–360, 1997.

[60] S. Prasanna and S. M. Spearing, "Materials selection and design of microelectrothermal bimaterial actuators," *Journal of Microelectromechanical Systems*, vol. 16, no. 2, pp. 248–259, 2007.

[61] K. H. Koh and C. Lee, "A low power 2-d raster scanning mems mirror driven by hybrid electrothermal and electromagnetic actuation mechanisms," in *Optical MEMS and Nanophotonics (OMN), 2012 International Conference on*, pp. 236–237, IEEE, 2012.

[62] L. Li, R. Bauer, G. Brown, and D. Uttamchandani, "A symmetric hybrid mems scanner with electrothermal and electrostatic actuators," in *Optical MEMS and Nanophotonics (OMN), 2011 International Conference on*, pp. 163–164, IEEE, 2011.

[63] U. Baran, D. Brown, S. Holmstrom, D. Balma, W. O. Davis, P. Muralt, and H. Urey, "Resonant pzt mems scanner for high-resolution displays," *Journal of Microelectromechanical Systems*, vol. 21, no. 6, pp. 1303–1310, 2012.

[64] C.-D. Chen, Y.-J. Wang, and P. Chang, "A novel two-axis mems scanning mirror with a pzt actuator for laser scanning projection," *Optics Express*, vol. 20, no. 24, pp. 27003–27017, 2012.

[65] P. Srinivasan and S. M. Spearing, "Optimal materials selection for bimaterial piezoelectric microactuators," *Journal of Microelectromechanical Systems*, vol. 17, no. 2, pp. 462–472, 2008.

[66] J. G. Smits, K. Fujimoto, and V. F. Kleptsyn, "Microelectromechanical flexure pzt actuated optical scanner: static and resonance behavior," *Journal of Micromechanics and Microengineering*, vol. 15, no. 6, p. 1285, 2005.

[67] T. Iseki, M. Okumura, and T. Sugawara, "High-speed and wide-angle deflection optical mems scanner using piezoelectric actuation," *IEEJ Transactions on Electrical and Electronic Engineering*, vol. 5, no. 3, pp. 361–368, 2010.

[68] J. Yan, S. Luanava, and V. Casasanta, "Magnetic actuation for mems scanners for retinal scanning displays," in *MOEMS Display and Imaging Systems*, vol. 4985, pp. 115–121, International Society for Optics and Photonics, 2003.

[69] A. D. Yalcinkaya, H. Urey, D. Brown, T. Montague, and R. Sprague, "Two-axis electromagnetic microscanner for high resolution displays," *Journal of Microelectromechanical Systems*, vol. 15, no. 4, pp. 786–794, 2006.

[70] J. Yan, S. Luanava, and V. Casasanta, "Magnetic actuation for mems scanners for retinal scanning displays," in *MOEMS Display and Imaging Systems*, vol. 4985, pp. 115–121, International Society for Optics and Photonics, 2003.

[71] R. A. Miller and Y.-C. Tai, "Micromachined electromagnetic scanning mirrors," *Optical Engineering*, vol. 36, no. 5, pp. 1399–1408, 1997.

[72] N. Asada, M. Takeuchi, V. Vaganov, N. Belov, S. in't Hout, and I. Sluchak, "Silicon micro-optical scanner," *Sensors and Actuators A: Physical*, vol. 83, no. 1-3, pp. 284–290, 2000.

[73] N. Asada, H. Matsuki, K. Minami, and M. Esashi, "Silicon micromachined two-dimensional galvano optical scanner," *IEEE Transactions on Magnetics*, vol. 30, no. 6, pp. 4647–4649, 1994.

[74] S.-H. Ahn and Y.-K. Kim, "Galvanometric silicon scanning mirror of 2 dof," in *Optical MEMs, 2002. Conference Digest. 2002 IEEE/LEOS International Conference on*, pp. 87–88, IEEE, 2002.

[75] A. Garnier, T. Bourouina, H. Fujita, E. Orsier, T. Masuzawa, T. Hiramoto, and J.-C. Peuzin, "A fast, robust and simple 2-d micro-optical scanner based on contactless magnetostrictive actuation," in *Micro Electro Mechanical Systems, 2000. MEMS 2000. The Thirteenth Annual International Conference on*, pp. 715–720, IEEE, 2000.

[76] R. A. Conant, J. T. Nee, K. Y. Lau, and R. S. Muller, "Dynamic deformation of scanning mirrors," in *Optical MEMS, 2000 IEEE/LEOS International Conference on*, pp. 49–50, IEEE, 2000.

[77] H. Kahn, R. Ballarini, J. Bellante, and A. Heuer, "Fatigue failure in polysilicon not due to simple stress corrosion cracking," *Science*, vol. 298, no. 5596, pp. 1215–1218, 2002.

[78] N. A. Moldovan, O. H. Auciello, A. Sumant, J. Carlisle, R. Divan, D. M. Gruen, A. R. Krauss, D. C. Mancini, A. Jayatissa, and J. Tucek, "Micromachining of ultrananocrystalline diamond," in *Micromachining and Microfabrication Process Technology VII*, vol. 4557, pp. 288–299, International Society for Optics and Photonics, 2001.

[79] K. Uchino, "Piezoelectric actuators," *Wiley Encyclopedia of Biomedical Engineering*, 2006.

[80] R. S. Fearing, "Powering 3 dimensional microrobots: Power density limitations," *Tutorial on Micro Mechatronics and Micro Robotics, ICRA*, vol. 98, 1998.

[81] C. Huang, J. Yao, L. V. Wang, and J. Zou, "A water-immersible 2-axis scanning mirror microsystem for ultrasound andha photoacoustic microscopic imaging applications," *Microsystem Technologies*, vol. 19, no. 4, pp. 577–582, 2013.

[82] J. Y. Kim, C. Lee, K. Park, G. Lim, and C. Kim, "A pdms-based 2-axis waterproof scanner for photoacoustic microscopy," *Sensors*, vol. 15, no. 5, pp. 9815–9826, 2015.

[83] O. Auciello, J. Birrell, J. A. Carlisle, J. E. Gerbi, X. Xiao, B. Peng, and H. D. Espinosa, "Materials science and fabrication processes for a new mems technology based on ultrananocrystalline diamond thin films," *Journal of Physics: Condensed Matter*, vol. 16, no. 16, p. R539, 2004.

[84] C. A. Van Eysden and J. E. Sader, "Resonant frequencies of a rectangular cantilever beam immersed in a fluid," *Journal of Applied Physics*, vol. 100, no. 11, p. 114916, 2006.

[85] L. V. Wang and S. Hu, "Photoacoustic tomography: in vivo imaging from organelles to organs," *Science*, vol. 335, no. 6075, pp. 1458–1462, 2012.

[86] H. F. Zhang, K. Maslov, G. Stoica, and L. V. Wang, "Functional photoacoustic microscopy for high-resolution and noninvasive in vivo imaging," *Nature Biotechnology*, vol. 24, no. 7, p. 848, 2006.

[87] A. D. Yalcinkaya, H. Urey, D. Brown, T. Montague, and R. Sprague, "Two-axis electromagnetic microscanner for high resolution displays," *Journal of Microelectromechanical Systems*, vol. 15, no. 4, pp. 786–794, 2006.

[88] W. Thomson, *Theory of vibration with applications*. CrC Press, 2018.

[89] I. E. E. Brandrup, J., "Handbook, polymer," 1989.

[90] W. M. Haynes, *CRC handbook of chemistry and physics*. CRC press, 2014.

[91] C. H. Frazier and W. D. O'Brien, "Synthetic aperture techniques with a virtual source element," *IEEE Transactions on Ultrasonics, Ferroelectrics, and Frequency Control*, vol. 45, no. 1, pp. 196–207, 1998.

[92] K. E. Petersen, "Silicon torsional scanning mirror," *IBM Journal of Research and Development*, vol. 24, no. 5, pp. 631–637, 1980.

[93] D. Dickensheets and G. Kino, "Micromachined scanning confocal optical microscope," *Optics Letters*, vol. 21, no. 10, pp. 764–766, 1996.

[94] K. H. Gilchrist, D. E. Dausch, and S. Grego, "Electromechanical performance of piezoelectric scanning mirrors for medical endoscopy," *Sensors and Actuators A: Physical*, vol. 178, pp. 193–201, 2012.

[95] A. D. Yalcinkaya, H. Urey, D. Brown, T. Montague, and R. Sprague, "Two-axis electromagnetic microscanner for high resolution displays," *Journal of Microelectromechanical Systems*, vol. 15, no. 4, pp. 786–794, 2006.

[96] L. Eldada, T. Yu, and A. Pacala, "Optical phased array lidar system and method of using same," June 9 2016. US Patent App. 14/279,348.

# APPENDIX A

## PHOTOLITHOGRAPHY PARAMETERS

1. PR AZ5214 process

Spin PR AZ5214 at 4000 rpm for 30 s.

Soft bake at $110°C$ hotplate for 30 s.

Expose for $100mJ/cm^2$.

Hard bake at $110°C$ hotplate for 45 s.

Develop in AZ400K developer until clear.

2. PR AZ9260 process

Spin PR AZ9260 at 3000 rpm for 30 s.

Soft bake at $110°C$ hotplate for 180 s.

Expose for $1200mJ/cm^2$.

Hard bake at $110°C$ hotplate for 45 s.

Develop in AZ400K developer until clear.

# APPENDIX B

## LASER MICROMACHINING PARAMETERS USING PLS6.75, UNIVERSAL LASER SYSTEM

1. BoPET film process

Laser power at 2%.

Laser speed at 4%.

Focal point at 1.5 in.

1200 DPI.

Suction at 5%.

2. Acrylic sheet process

Laser power at 6%.

Laser speed at 3%.

Focal point at 1.5 in.

1200 DPI.

Suction at 45%.

# APPENDIX C

## FABRICATION RECIPE OF MINIATURIZED TWO-AXIS WATER-IMMERSIBLE SCANNING MIRROR

1. Substrate preparation

$200\mu m$ DSP silicon wafer, $50\mu m$ BoPET film sheet, cleaned with acetone, IPA, and DI water.

2. Al evaporation step 1

Evaporate 200 nm Al on the silicon wafer surface.

3. PR step 1

PR AZ5214 process on Al surface for alignment marks patterning.

4. Al etch

Etch the alignment marks on the Al mask.

5. Silicon etch

Thorough etch the alignment marks.

6. Al mask removal

Remove Al mask.

7. Cr evaporation

Evaporate 10 nm Cr on the silicon wafer surface.

8. Bonding agency spin

Spin NOA81 optical adhesive on Cr surface at 1000 rpm for 30 s.

9. Silicon to BoPET bonding

Bond BoPET sheet to silicon wafer surface with spun bonding agency.

10. Bonding agency curing

After removing bubbles in the bonding agency, expose the bonding agency for $2J/cm^2$.

11. Cr/Cu evaporation as seed layer

Cr: 10 nm at 1 nm/min, Cu: 200 nm at 2 nm/min on the BoPET surface.

12. PR step 2

PR AZ9260 process on the Cr/Cu surface.

13. Ni mask electroplating

Electroplate Ni at 5 $\mu m$.

14. PR removal

Remove PR 2 with acetone, IPA, and DI water.

15. Cu etch

Cu etch in ($HAC$:$H_2O_2$:$H_2O$=1:1:10) until clear.

16. Cr etch

Cr etch in ($HCl$:$H_2O$=1:10) initiated by aluminum foil until clear.

17. BoPET cryogenic etching

Through etch BoPET sheet.

18. Al evaporation

Evaporte 200 nm Al on silicon surface.

19. PR step 3

PR AZ5214 process on Al surface for alignment marks patterning.

19. Al etch

Etch the alignment marks on the Al mask.

20. Silicon etch

Thorough etch the silicon wafer.

21. Permanent magnet bonding

Bond permanent magnets onto the backside of BoPET sheet with a template.

22. Acrylic spacer and inductor coil bonding

Bond acrylic spacers and inductor coil to the backside of BoPET layer.

# APPENDIX D

## NI ELECTROPLATING SOLUTION

$NaCl$: 25g/L

$NiCl$: 19.5g/L

$NiSO_4$: 8.15g/L

$H_3BO_4$: 12.5g/L

$SodiumSaccharin$: 0.75g/L

Adjust pH to 4.7